

# Partial-wave analyses of $\gamma p \rightarrow \eta p$ and $\gamma n \rightarrow \eta n$ using a multichannel framework

B. C. Hunt and D. M. Manley

*Department of Physics, Kent State University, Kent, OH 44242-0001, USA*

(Dated: June 5, 2022)

This paper presents results from partial-wave analyses of the photoproduction reactions  $\gamma p \rightarrow \eta p$  and  $\gamma n \rightarrow \eta n$ . World data for the observables  $d\sigma/d\Omega$ ,  $\Sigma$ ,  $T$ ,  $P$ ,  $F$ , and  $E$  were analyzed as part of this work. The dominant amplitude in the fitting range from threshold to a c.m. energy of 1900 MeV was found to be  $S_{11}$  in both reactions, consistent with results of other groups. At c.m. energies above 1600 MeV, our solution deviates from published results, with this work finding higher-order partial waves becoming significant. Data off the proton suggest that the higher-order terms contributing to the reaction include  $P_{11}$ ,  $P_{13}$ , and  $F_{15}$ . The final results also hint that  $F_{17}$  is needed to fit double-polarization observables above 1900 MeV. Data off the neutron show a contribution from  $P_{13}$ , as well as strong contributions from  $D_{13}$  and  $D_{15}$ .

## I. INTRODUCTION

In recent years, a wealth of new high-precision experimental data has been measured at various facilities including JLab, MAMI, LEPS, SLAC, and GRAAL for a number of observables with the goal of better understanding the spectrum of  $N^*$  and  $\Delta^*$  resonances. Despite past efforts, there are still predicted resonances that have not been found, known as the problem of the “missing resonances”, and other resonances whose properties are not well determined. Two possible explanations for this are that (1) the missing resonances do not exist or (2) they couple mainly to reactions not yet analyzed. This work investigates the second possibility. Knowledge gained from this and future work is expected to guide theorists trying to understand the fundamental features of Quantum Chromodynamics (QCD) or the theory of the quarks and gluons that bind matter into hadrons.

It is well known that at least eight measured observables are needed to perform a complete experiment [1]. The database analyzed in this work for  $\gamma p \rightarrow \eta p$  and  $\gamma n \rightarrow \eta n$  include significant amounts of data for five of the eight needed observables. These five are  $d\sigma/d\Omega$ ,  $\Sigma$ ,  $T$ ,  $F$ , and  $E$  measured at various c.m. energies from threshold to 1900 MeV. Also analyzed were seven  $P$  and 12  $C_{x'}$  data points. Data for the helicity-dependent cross section were analyzed as  $d\sigma/d\Omega$  and  $E$  data. Table I tabulates the number of data available for each observable and shows that while there are a wealth of differential cross-section data, the polarization measurements are still limited. Because there are still insufficient data for a complete experiment, information from other reactions, including  $\gamma N \rightarrow \pi N$  and  $\pi N \rightarrow \eta N$ , was used to constrain the fits.

This work analyzed the world data of eta photoproduction off the nucleon in the c.m. energy range from threshold up to almost 2000 MeV. The final generated energy-dependent solutions were then used in the KSU multichannel framework to improve knowledge about the  $N^*$  and  $\Delta^*$  resonance parameters. Section II outlines the basic formalism used throughout this work including sign conventions for the different spin observables. Section III describes the general procedure that we used to obtain

Observable	$\gamma p \rightarrow \eta p$	$\gamma n \rightarrow \eta n$
$d\sigma/d\Omega$	7754	879
$T$	439	96
$\Sigma$	236	80
$P$	7	0
$E$	331	135
$F$	241	96
$C_{x'}$	12	0

TABLE I. Number of experimental data used in our analysis for each fitted observable.

the results. Section IV describes results of the analyses for the reactions  $\gamma p \rightarrow \eta p$  and  $\gamma n \rightarrow \eta n$ . Comparisons to results from BnGa (2016) [2] and Jülich (2015) [3] are also shown. Fits to the data are shown in Appendix A.

## II. FORMALISM

Four helicity amplitudes are needed to describe the photoproduction of a pseudoscalar ( $J^P = 0^-$ ) meson and a  $J^P = \frac{1}{2}^+$  baryon off of a nucleon target [4]. Each of the four helicity amplitudes can be expanded in terms of electric and magnetic multipoles  $E_{l\pm}$  and  $M_{l\pm}$ , respectively, where  $l = 0, 1, 2, \dots$  is the orbital angular momentum of the final-state hadrons and  $j = l \pm \frac{1}{2}$  is the total angular momentum. Each multipole is a complex function of energy, which makes the helicity amplitudes complex functions of both energy and scattering angle:

$$H_N = \sqrt{\frac{1}{2}} \cos\left(\frac{\theta}{2}\right) \sum_{l=0}^{\infty} [(l+2) E_{l+} + l M_{l+} + l E_{(l+1)-} - (l+2) M_{(l+1)-}] (P'_l - P'_{l+1}), \quad (1a)$$

$$H_{SP} = \sqrt{\frac{1}{2}} \cos\left(\frac{\theta}{2}\right) \sin(\theta) \sum_{l=1}^{\infty} [E_{l+} - M_{l+}] - E_{(l+1)-} - M_{(l+1)-}] (P''_l - P''_{l+1}), \quad (1b)$$

Observable	Expt.
$\sigma(\theta) = \frac{q}{2k} [ H_N ^2 +  H_D ^2 +  H_{SA} ^2 +  H_{SP} ^2]$	
$\Sigma \sigma(\theta) = \frac{q}{k} \text{Re}[H_{SP}H_{SA}^* - H_NH_D^*]$	<i>B</i>
$T \sigma(\theta) = \frac{q}{k} \text{Im}[H_{SP}H_N^* + H_DH_{SA}^*]$	<i>T</i>
$P \sigma(\theta) = -\frac{q}{k} \text{Im}[H_{SP}H_D^* + H_NH_{SA}^*]$	<i>R</i>
$G \sigma(\theta) = -\frac{q}{k} \text{Im}[H_{SP}H_{SA}^* + H_NH_D^*]$	<i>B, T</i>
$H \sigma(\theta) = -\frac{q}{k} \text{Im}[H_{SP}H_D^* + H_{SA}H_N^*]$	<i>B, T</i>
$F \sigma(\theta) = \frac{q}{k} \text{Re}[H_{SA}H_D^* + H_{SP}H_N^*]$	<i>B, T</i>
$E \sigma(\theta) = \frac{q}{2k} [ H_N ^2 +  H_{SA} ^2 -  H_D ^2 -  H_{SP} ^2]$	<i>B, T</i>

TABLE II. List of single-polarization and double-polarization observables analyzed in this work. See Refs. [4, 6] for a detailed description of the necessary experimental setup and equations for all 16 observables. In the second column, *B*, *T*, and *R* refer to a measurement of the beam, target, and recoil nucleon polarization, respectively. Note that  $\sigma(\theta) = d\sigma/d\Omega$  is the differential cross section.

$$H_{SA} = \sqrt{\frac{1}{2}} \sin\left(\frac{\theta}{2}\right) \sum_{l=0}^{\infty} [(l+2) E_{l+} + l M_{l+} - l E_{(l+1)-} + (l+2) M_{(l+1)-}] (P_l' + P_{l+1}'), \quad (1c)$$

$$H_D = \sqrt{\frac{1}{2}} \sin\left(\frac{\theta}{2}\right) \sin(\theta) \sum_{l=1}^{\infty} [E_{l+} - M_{l+} + E_{(l+1)-} + M_{(l+1)-}] (P_l'' + P_{l+1}''). \quad (1d)$$

The naming convention for the four helicity amplitudes above follows that of the SAID group [5]. All 16 single- and double-polarization observables can be written in terms of these four helicity amplitudes; however, in the literature, different sign conventions are used in their definitions. The definitions for each of the observables included in this work are given in Table II.

The literature also mentions measurements of  $(d\sigma/d\Omega)_{\frac{1}{2}}$  and  $(d\sigma/d\Omega)_{\frac{3}{2}}$ , which are the helicity-dependent cross sections [7]. They are related to the  $d\sigma/d\Omega$  and  $E$  observables by

$$\frac{d\sigma}{d\Omega_{\frac{1}{2}}} = \frac{d\sigma}{d\Omega} + E \frac{d\sigma}{d\Omega} \propto |H_N|^2 + |H_{SA}|^2 \quad (2)$$

and

$$\frac{d\sigma}{d\Omega_{\frac{3}{2}}} = \frac{d\sigma}{d\Omega} - E \frac{d\sigma}{d\Omega} \propto |H_{SP}|^2 + |H_D|^2. \quad (3)$$

$H_N$  and  $H_{SA}$  are then pure helicity-1/2 amplitudes, while  $H_{SP}$  and  $H_D$  are pure helicity-3/2 amplitudes. The full differential cross section is recovered by the relationship

$$\frac{d\sigma}{d\Omega} = \frac{1}{2} \left[ \frac{d\sigma}{d\Omega_{\frac{1}{2}}} + \frac{d\sigma}{d\Omega_{\frac{3}{2}}} \right]. \quad (4)$$

Equations 2 and 3 can be separately integrated to obtain what are called the helicity-1/2 and helicity-3/2 cross sections, which are shown in Figs. 2 and 3.

### III. FITTING PROCEDURE

We began our analysis by performing single-energy partial-wave analyses. The starting point was to assemble all data within specified small c.m. energy ranges into individual bins. Observables within a single bin were then approximated as functions of just the scattering angle. It was determined that 5-MeV wide bins were needed near threshold where the  $S_{11}$  amplitude dominates due to the rapid rise in the cross section near the  $S_{11}(1535)$  resonance. At c.m. energies above  $W \approx 1600$  MeV, a trade-off between small bin sizes and keeping sufficient polarization data within the energy bin meant that larger bin sizes of 15 to 20 MeV were needed to constrain the fits.

Once the data were binned, the global phase was initially determined by first fitting the data with a purely real  $S_{11}$  amplitude to determine its magnitude. Then an energy-dependent fit, similar to those of Shrestha and Manley [8], was used to determine its phase through unitarity constraints. With the  $S_{11}$  amplitude fully determined, initial values for the higher-order amplitudes could then be determined.

Due to complexities that arise from interference effects, an iterative procedure was needed to obtain good quality fits to the data. The procedure involved two main steps that were iterated as many times as necessary to obtain convergence. The first step (single-energy fits) was to allow a subset of the partial-wave amplitudes to vary in each energy bin. This generated a discrete solution for each of the varied partial-wave amplitudes. These single-energy results were then used as input to energy-dependent fits (the second step) that were also used to determine the resonance parameters. In this second step, resonance parameters were adjusted to generate a smooth energy-dependent solution of the single-energy amplitudes. Finally, the output of the second step was used as input to the first step. This iterative procedure was continued until  $\chi^2$  reached a global minimum for this and all other analyzed reactions in the energy-dependent analysis, which included  $\gamma N \rightarrow \pi N$  and  $\gamma p \rightarrow K\Lambda$  as well as  $\pi N \rightarrow \pi N$ ,  $\pi N \rightarrow \pi\pi N$ ,  $\pi N \rightarrow \eta N$ , and  $\pi N \rightarrow K\Lambda$ . This means the final binned solutions found as part of this work are within a few percent, but not at, the exact minimum for the reaction.

Because not all measured observables are available in all energy bins, a penalty term was added to the standard  $\chi^2$  term to constrain the bin-to-bin solution. The explicit form for the penalty term was

$$\chi_{\text{penalty}}^2 = \frac{(PW_{\text{ED}} - PW_{\text{FIT}})^2}{\sigma^2}, \quad (5)$$

where  $PW_{\text{ED}}$  is the starting value found in step two of

the iterative process and  $PW_{FIT}$  are the amplitudes that were varied to improve the fits further. This biased results to single-energy solutions that were somewhat similar to the current energy-dependent solution.  $\sigma$  was a parameter that was chosen to control the strength of the constraints, with smaller values more tightly constraining the fits. To minimize bias from the penalty term, multiple starting solutions were used to determine which produced the best fit.

Once the solution converged to a minimum, final uncertainties on the amplitudes in the single-energy solutions from step one were obtained by fixing the phases of each partial-wave amplitude at the values from our energy-dependent solution, and then allowing only their moduli to vary. This phase constraint was needed to fix both the global phase of the solution and to constrain the final results due to lack of all spin observables at all energies. An additional penalty constraint was used as well, but kept small enough that the penalty contribution to  $\chi^2$  was less than 10%. The resulting single-energy solutions, projected into real and imaginary parts, were then used as input to a final energy-dependent fit in which all parameters were free to vary, to determine final uncertainties in the  $N^*$  and  $\Delta^*$  resonance parameters. Our final fits included all amplitudes up to  $G_{17}$  for both  $\gamma p \rightarrow \eta p$  and  $\gamma n \rightarrow \eta n$ , although  $F_{17}$  was the highest amplitude necessary for good fits.

#### IV. RESULTS

This section presents final results for the partial-wave analyses of both  $\gamma p \rightarrow \eta p$  and  $\gamma n \rightarrow \eta n$ . It compares results with those of other groups and shows the quality of agreement for the integrated cross-section data that were not directly fitted.

##### A. $\gamma p \rightarrow \eta p$

For the reaction  $\gamma p \rightarrow \eta p$ , the fits of the observables  $d\sigma/d\Omega$ ,  $T$ ,  $F$ , and  $E$  were very good over the entire energy range; however, the fits of the beam asymmetry  $\Sigma$  showed minor problems at backward angles in the c.m. energy range 1650 to 1800 MeV. Table III shows the  $\chi^2$  contribution from each individual observable for the different works as well as the total over all observables. We note that the  $\chi^2$  contribution from the differential cross section obtained in this work is significantly smaller than that by other groups with minimal impact to the spin observables. This is in part because we included in our fits new high-precision data for some observables that were unavailable to the other groups at their time of analyses. In order to provide a good description of the data, the amplitudes  $S_{11}$  and  $D_{13}$  were needed starting at threshold and  $P_{11}$ ,  $P_{13}$ , and  $F_{15}$  waves were important above 1600 MeV. At energies above 1900 MeV,  $F_{17}$  appears important, but the lack of spin observables at

these energies made it difficult to make any definitive conclusions. The magnitude of  $S_{11}$  partial-wave amplitude above 1600 MeV was found to differ from the results of BnGa [2], which found  $S_{11}$  saturating the integrated cross section over almost the entire energy range analyzed in this work.

Observable	KSU	BnGa (2016)	Jülich (2015b)
$d\sigma/d\Omega$	44000	83000	58000
$T$	1500	1200	900
$\Sigma$	950	380	1100
$F$	680	480	340
$E$	620	690	1300
$C_{x'}$	16	20	30
$(d\sigma/d\Omega)_{\frac{1}{2}}$	810	550	1300
$(d\sigma/d\Omega)_{\frac{3}{2}}$	200	250	350
Fit Total	50000	87000	64000

TABLE III.  $\chi^2$  contributions for  $\gamma p \rightarrow \eta p$ . Column 1 provides the observable name, column 2 the  $\chi^2$  contribution from this work, column 3 the  $\chi^2$  contribution from BnGa (2016) [2] and column 4 the  $\chi^2$  contribution from Jülich (2015b) [3].  $\chi^2$  values, were obtained by binning the data in 5-MeV increments in the full c.m. energy range from 1490 to 1975 MeV.

The integrated cross section ( $\sigma$ ) was obtained by integrating the differential cross section over the full angular range. The helicity-1/2 and 3/2 cross sections were generated by integrating the helicity-dependent differential cross-section data as defined in Eqs. (2) and (3). Figures 1, 2, and 3 show the full integrated cross section as well as the helicity-1/2 and 3/2 integrated cross sections. The curves generated through the integrated cross section points were obtained by fitting the differential cross section data and extracting the integrated cross section from the individual partial-wave amplitudes. Overall, the curves describe the data well through the entire energy region. The curve for  $\sigma$  slightly overshoots the data near 1600 MeV but our fits to  $d\sigma/d\Omega$  data were found to be in good agreement. The helicity-1/2 and helicity-3/2 plots also showed good agreement within experimental uncertainty and the scatter in the points.

Figure 4 compares the  $\gamma p \rightarrow \eta p$  partial-wave amplitudes from this work with results from BnGa [2] and Jülich [3]. For this reaction, the only amplitude that is in agreement between all the groups is  $S_{11}$ . Higher partial waves all exhibit major discrepancies with at least one of the groups. This lack of agreement indicates that additional data are needed from unmeasured double polarization observables to obtain a unique solution.

To obtain further progress towards the goal of a single solution for  $\eta$  photoproduction off the nucleon, Fig. 5 shows what observables show the most difference between the three groups compared in this work. A measurement

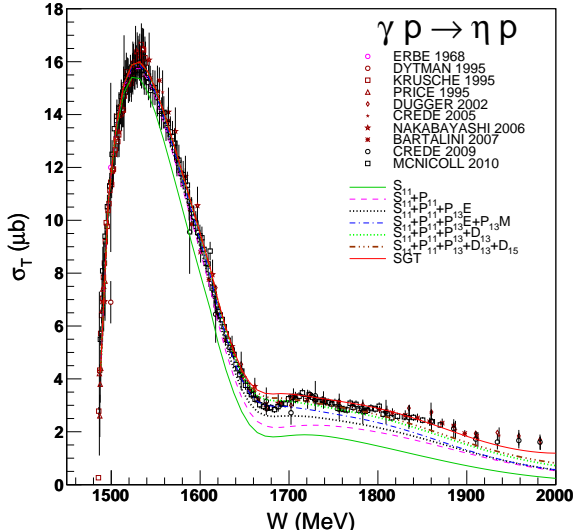


FIG. 1. Integrated cross section for  $\gamma p \rightarrow \eta p$ . The data points are from ERBE 1968 [9], DYTMAN 1995 [10], KRUSHE 1995 [11], PRICE 1995 [12], DUGGER 2002 [13], CREDE 2005 [14], NAKABAYASHI 2006 [15], BARTALINI 2007 [16], CREDE 2009 [17], and MCNICOLL 2010 [18]. The curves also show the contribution to the cross section by successively adding each partial wave.

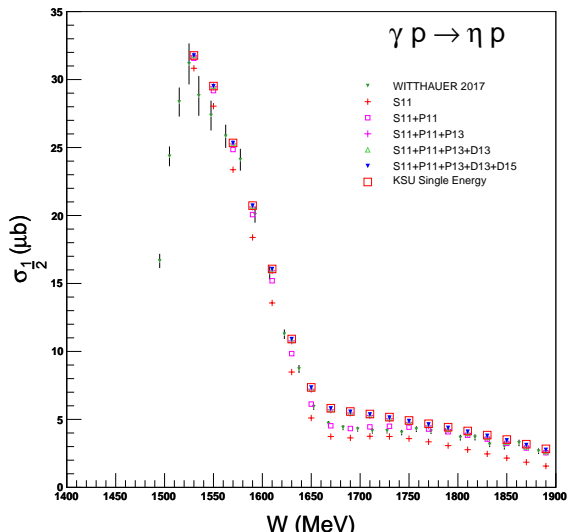


FIG. 2. Helicity-1/2 integrated cross section for  $\gamma p \rightarrow \eta p$ . The data points are from Witthauer 2017 [7]. The plot also shows the contribution to the cross section by successively adding each partial wave.

of both  $C_{x'}$  and  $C_{z'}$  would be ideal at c.m. energies between 1600 and 1800 MeV while above 1800, the predictions for these two observables actually converge and a better measurement would be either  $G$  or  $H$ .

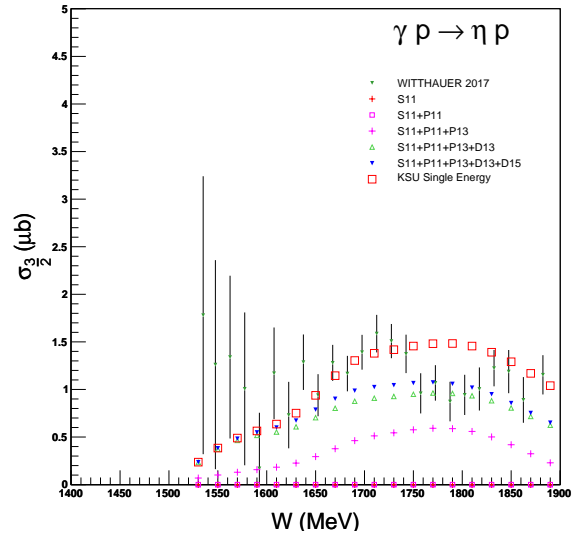


FIG. 3. Helicity-3/2 integrated cross section for  $\gamma p \rightarrow \eta p$ . The data points are from Witthauer 2017 [7]. The plot also shows the contribution to the cross section by successively adding each partial wave.

## B. $\gamma n \rightarrow \eta n$

For the reaction  $\gamma n \rightarrow \eta n$ , our fits to the published observables  $d\sigma/d\Omega$ ,  $E$ , and  $\Sigma$  are overall very good. Fits to the  $E$  observable are overall quite good with just a few bins showing minor local problems. Using wide binning showed that the data varied significantly from bin-to-bin, which prevented further improvements to the fits. The  $S_{11}$  amplitude dominates the reaction from threshold up to 1620 MeV, with  $P_{13}E$  and  $D_{15}$  showing significant contributions in the region of the narrow structure near 1680 MeV. Table IV lists shows the  $\chi^2$  contributions for this work and BnGa (2016) [2]. Again, individual and total contributions are shown. This work does a slightly better job at describing a few of the observables while BnGa (2016) does better at others. It is noted that BnGa did not have available the data for the observables  $T$ ,  $F$ , and  $E$ .

Figures 6, 7, and 8 show integrated cross-section results. Both Figs. 6 and 7 reveal what appears to be a narrow structure less than 100 MeV wide near 1680 MeV. Much has been written about this structure. Some researchers have concluded that the bump must be from either a  $P_{11}$  resonance or due to an interference effect between two  $S_{11}$  resonances [19, 20] because the structure only appears in the helicity-1/2 data (see Figs. 7 and 8). The argument has been made that the helicity-1/2 cross section contains contributions from  $S_{11}$  and  $P_{11}$ , while the helicity-3/2 cross section does not, so the bump must be due to these two amplitudes.

The present work provides an alternative interpretation of the bump as a complicated structure generated by a number of resonances, specifically  $D_{13}(1700)$ ,  $D_{15}(1675)$ , and the tail of the  $S_{11}(1535)$ . As mentioned

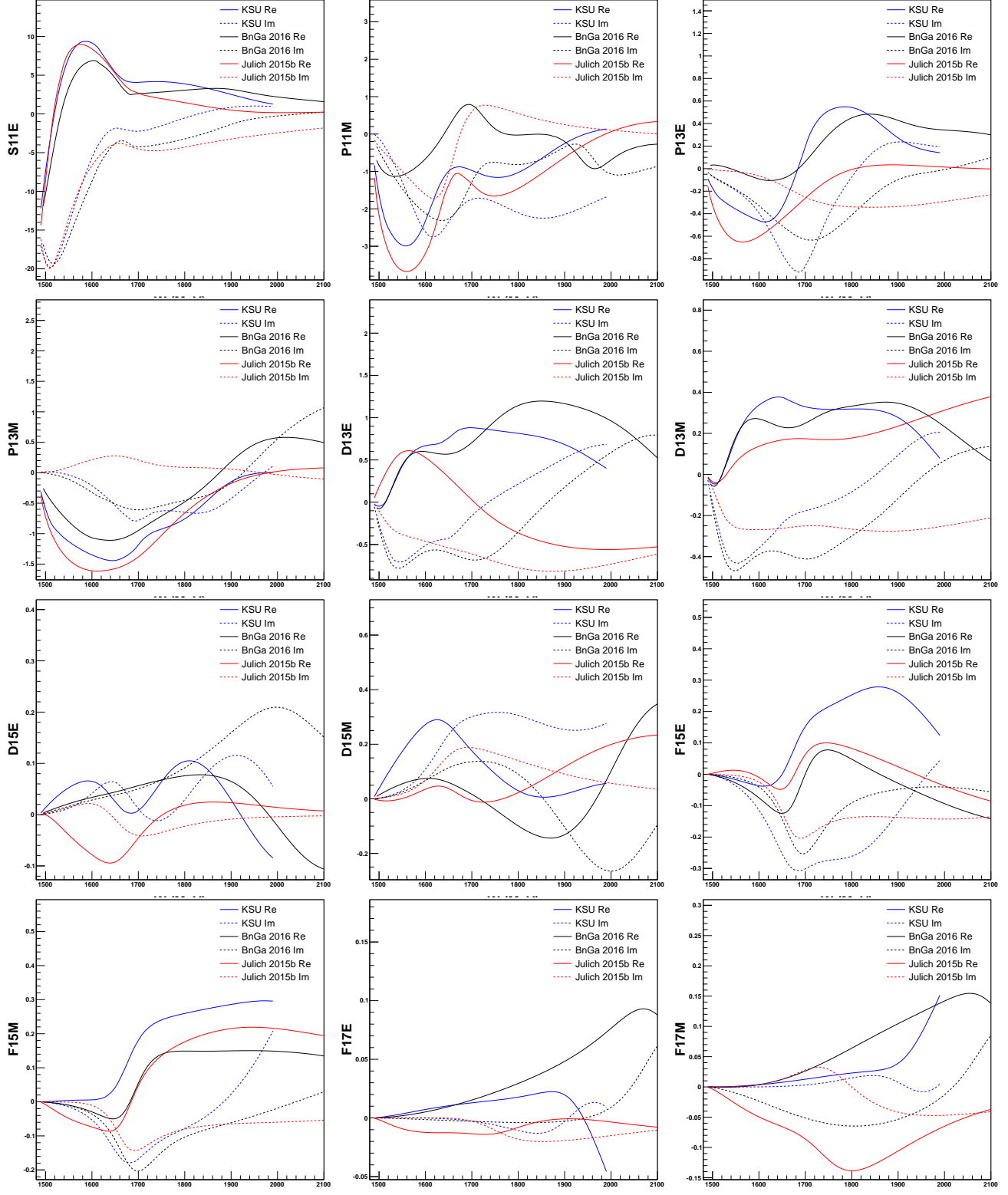


FIG. 4. Comparison of the individual  $\gamma p \rightarrow \eta p$  partial-wave amplitudes for each group. Blue, black, and red curves are from this work, BnGa [2], and Julich [3], respectively. The solid curves are the real parts and the dotted curves are the imaginary parts of the amplitudes. The amplitudes are in units of mfm.

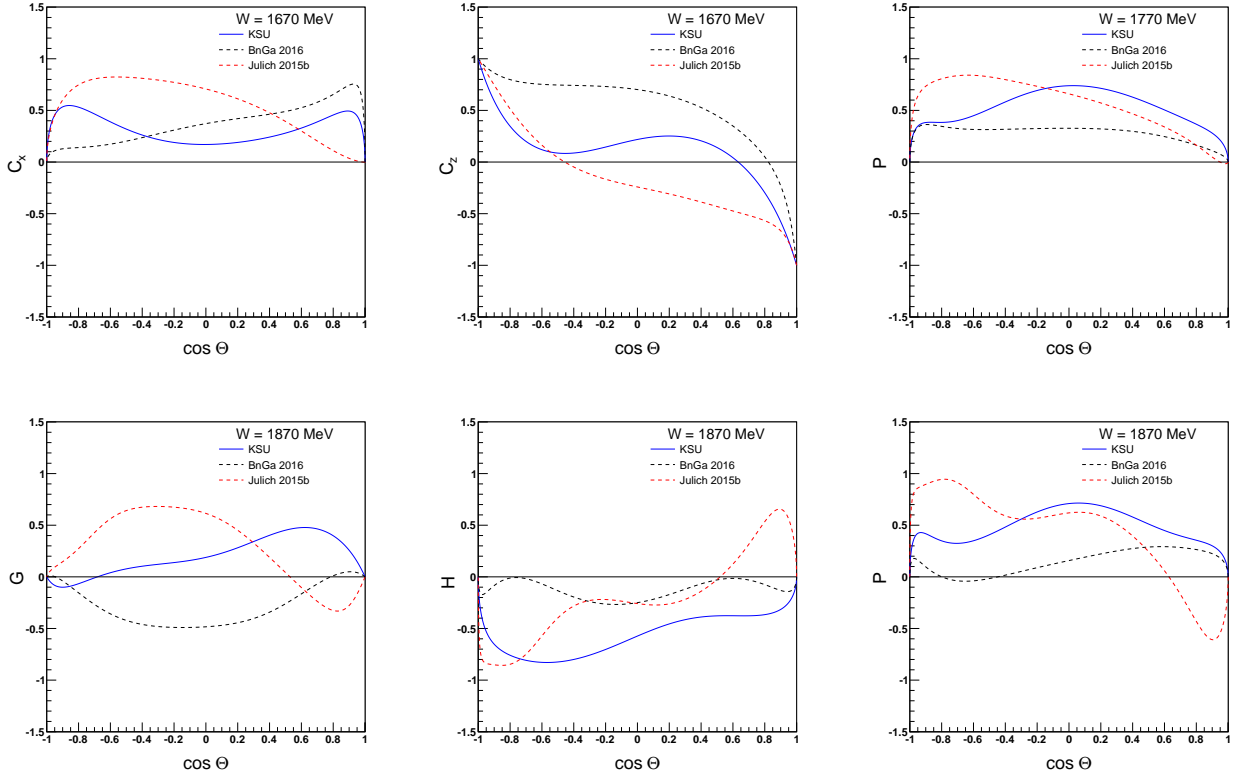


FIG. 5. Predictions of  $C_{x'}$ ,  $C_{z'}$ ,  $G$ ,  $H$ , and  $P$  at various energies for the reaction  $\gamma p \rightarrow \eta p$ . Measurement of any of these observables at the shown energy would provide strong evidence for any needed changes in the three works results. The top two plots on the left are for  $C_{x'}$  and  $C_{z'}$ , respectively, at a c.m. energy of 1670 MeV. The top right plot is for  $P$  at 1770 MeV, and the bottom three plots are for  $G$ ,  $H$ , and  $P$ , respectively, at 1870 MeV. The blue solid curves are from this work, the black dotted curves are from BnGa [2], and the red dotted curves are from Julich [3].

Observable	KSU	BnGa (2016)
$d\sigma/d\Omega$	6300	6800
$T$	480	700
$\Sigma$	240	200
$F$	220	440
$E$	250	150
$(d\sigma/d\Omega)_{\frac{1}{2}}$	310	260
$(d\sigma/d\Omega)_{\frac{3}{2}}$	210	140
Fit Total	8100	8700

TABLE IV.  $\chi^2$  contributions for  $\gamma n \rightarrow \eta n$ . Column 1 shows the name of the observable, columns 2 and 3 show the  $\chi^2$  contributions from this work and BnGa (2016) [2], respectively. The c.m. energy range was from 1490 to 1875 MeV with 5 MeV binning.

above, this would generate a bump in the helicity-3/2 cross section. Our predictions of the helicity cross sections (Figs. 7 and 8) show that the data allow and even

hint at a small bump within the size of the error bars and scatter of the points. While the fits to the integrated cross section seem to overshoot the data at c.m. energies near 1650 MeV, the energy resolution in the region around the bump is 30 MeV (and wider at higher energies), despite the cross section points being roughly 10 MeV apart [21].

Plots comparing the  $\gamma n \rightarrow \eta n$  partial-wave amplitudes determined in this work with BnGa results [2] are shown in Figure 9. The  $S_{11}$  amplitude is similar except in the c.m. energy region near 1680 MeV where the BnGa group explains the bump as an  $S_{11}$  interference and what looks like a cusp effect, possibly from the opening of the  $K\Sigma$  channel near 1680 MeV. The only other amplitude that is similar between the two groups is the  $D_{13}E$  amplitude.

In our fits, there appears to be more structure than that found in the BnGa solution. Resonance peaks are clearly seen in multiple amplitudes with the imaginary part of the amplitude forming a peak when the corresponding real part approaches zero, as expected for a Breit-Wigner resonance.

At this point, additional measurements of any of the 16 observables would be useful to constrain the fits fur-

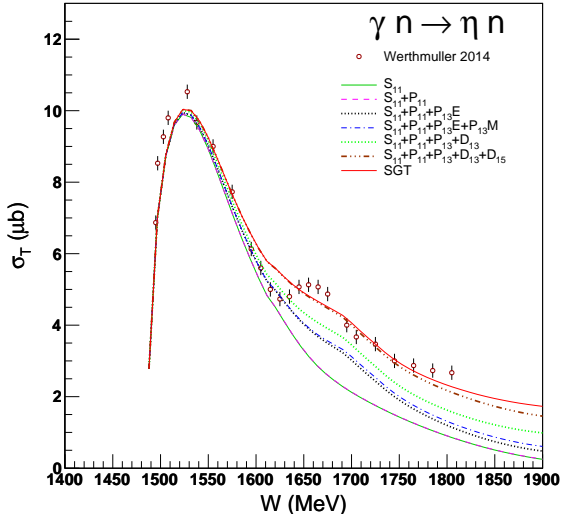


FIG. 6. Integrated cross section for  $\gamma n \rightarrow \eta n$ . The curves show the contribution to the cross section by successively adding each partial wave.

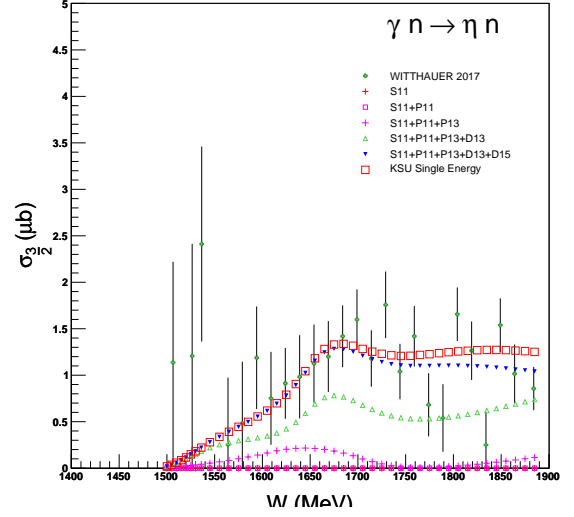


FIG. 8. Helicity-3/2 integrated cross section for  $\gamma n \rightarrow \eta n$ . The data points are from Witthauer 2017 [7] and the plot also shows the contribution to the cross section by successively adding each partial wave.

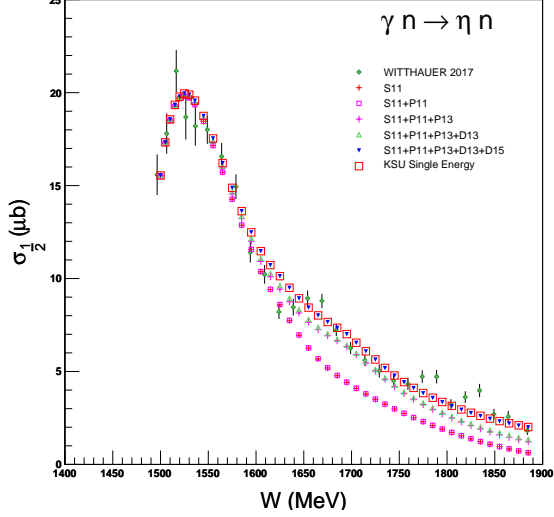


FIG. 7. Helicity-1/2 integrated cross section for  $\gamma n \rightarrow \eta n$ . The data points are from Witthauer 2017 [7] and the plot also shows the contribution to the cross section by successively adding each partial wave.

ther and confirm previous measurements. As such, no predictions are shown at this point.

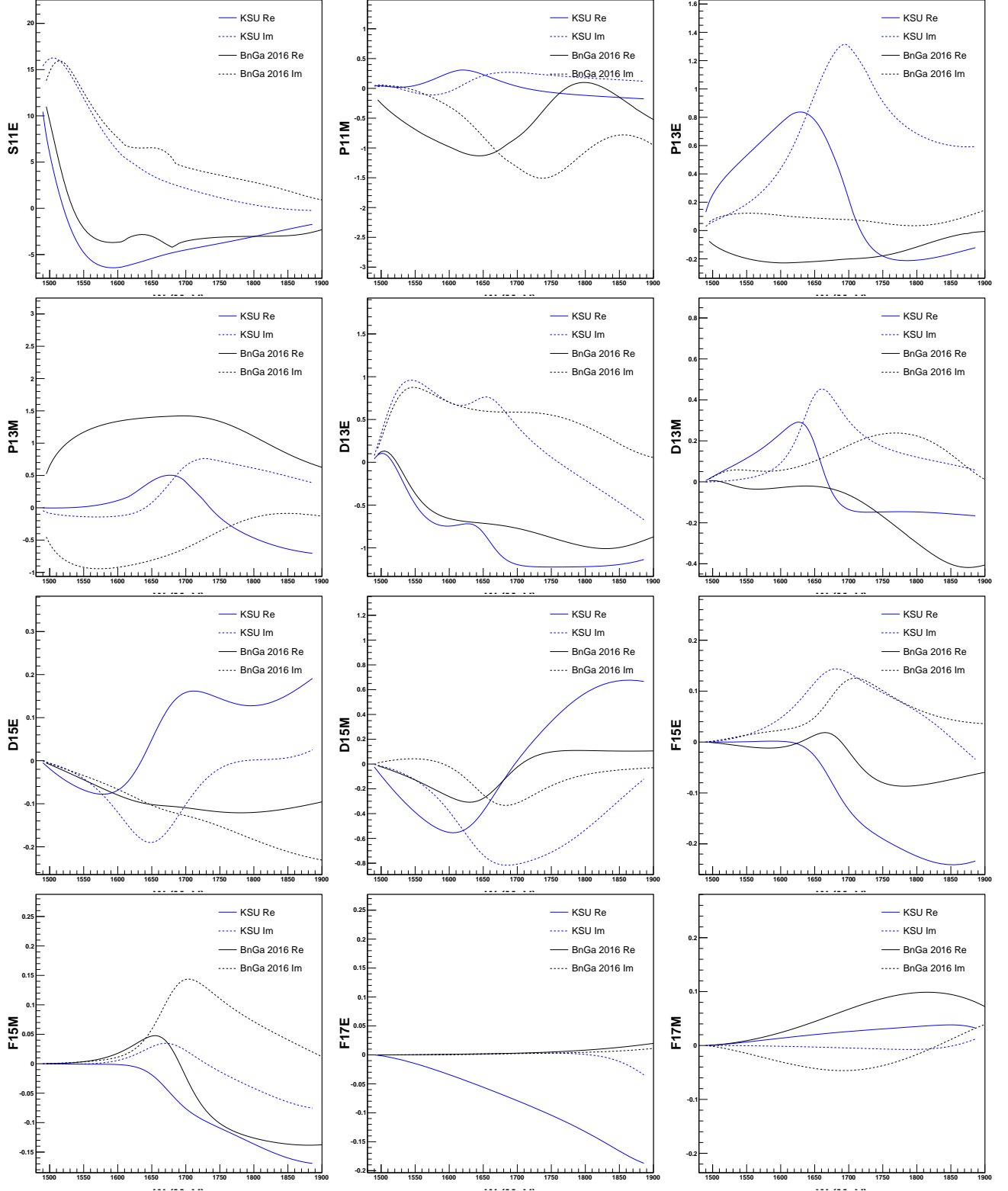


FIG. 9. Comparison of the individual  $\gamma n \rightarrow \eta n$  partial-wave amplitudes for each group. The blue and black curves are from this work and BnGa [2], respectively. The solid curve is the real part and the dotted curve the imaginary part of the amplitude. The amplitudes are in units of mfm.

## V. SUMMARY AND CONCLUSIONS

Results from a partial-wave analysis of available data for  $\gamma N \rightarrow \eta N$  were presented.  $S_{11}$ ,  $P_{11}$ ,  $P_{13}$ , and  $F_{15}$  amplitudes were found to be important for the reaction  $\gamma p \rightarrow \eta p$  in the energy range from threshold to 2000 MeV.  $S_{11}$ ,  $P_{13}$ ,  $D_{13}$ , and  $D_{15}$  were important for  $\gamma n \rightarrow \eta n$ . This is consistent with the Moorhouse selection rule [22], which predicts that the  $D_{15}(1675)$  resonance may couple to  $\gamma n$  but not to  $\gamma p$ .

Also, despite the wealth of new data, measurements of additional double polarization measurements are still

needed to obtain agreement between the different partial-wave analyses.

## ACKNOWLEDGMENTS

The authors would like to thank Igor Strakovsky for supplying much of the database. This work was supported in part by the U.S. Department of Energy, Office of Science, Office of Nuclear Physics Research Division, under Awards No. DE-FG02-01ER41194 and DE-SC0014323, and by the Department of Physics at Kent State University.

- 
- [1] W. Chiang and F Tabakin, Phys. Rev. C **55**, 2054 (1997).  
[2] A. Sarantsev, private communication (2017).  
[3] D. Rönchen *et al.*, Eur. Phys. J. A **51**, 70 (2015).  
[4] I. S. Barker, A. Donnachie, and J. K. Storrow, Nucl. Phys. B **95**, 347 (1975).  
[5] R. Arndt *et al.*, Phys. Rev. C **42**, 1853 (1990).  
[6] A. Sandorfi, S. Hoblit, H. Kamano, and T. S. H. Lee, arXiv:1010.4555v2 [nucl-th].  
[7] L. Witthauer *et al.*, Phys. Rev. C **95**, 55201 (2017).  
[8] M. Shrestha and D. M. Manley, Phys. Rev. C **86**, 055203 (2012).  
[9] R. Erbe *et al.*, Phys. Rev. **175**, 1669 (1968).  
[10] S. A. Dytman *et al.*, Phys. Rev. C **51**, 2710 (1995).  
[11] B. Krushe *et al.*, Phys. Rev. Lett. **74**, 3736 (1995).  
[12] J. W. Price *et al.*, Phys. Rev. C **51**, R2283 (1995).  
[13] M. Dugger *et al.*, Phys. Rev. Lett. **89**, 222002 (2002).  
[14] V. Crede *et al.*, Phys. Rev. Lett. **94**, 12004 (2005).  
[15] T. Nakabayashi *et al.*, Phys. Rev. C **74**, 35202 (2006).  
[16] O. Bartalini *et al.*, Eur. Phys. J. A **33**, 169 (2007).  
[17] V. Crede *et al.*, Phys. Rev. C **80**, 55202 (2009).  
[18] E. McNicoll *et al.*, Phys. Rev. C **82**, 35208 (2010).  
[19] V. Kuznetsov *et al.*, Acta Phys. Polon. B **39**, 1949 (2008).  
[20] A. V. Anisovich *et al.*, arXiv 1501.02093 [nucl-ex].  
[21] D. Werthmüller *et al.*, Phys. Rev. C **90**, 15205 (2014).  
[22] R. G. Moorhouse, Phys. Rev. Lett. **16**, 772 (1966).  
[23] See supplemental material at [url provided by PRC] for data files containing all the partial-wave amplitudes described in this paper.  
[24] C. A. Heusch, C. Y. Prescott, E. D. Bloom, and L. S. Rochester, Phys. Rev. Lett. **17**, 573 (1966).  
[25] R. Prepost, D. Lundquist, and D. Quinn, Phys. Rev. Lett. **18**, 82 (1967).  
[26] C. Bacci *et al.*, Phys. Rev. Lett. **20**, 571 (1968).  
[27] E. D. Bloom, C. A. Heusch, C. Y. Prescott, and L. S. Rochester, Phys. Rev. Lett. **21**, 1100 (1968).  
[28] B. Delcourt *et al.*, Phys. Lett. B **29**, 75 (1969).  
[29] J. R. Holt *et al.*, Daresbury Nuclear Physics Laboratory preprint DNPL, 69 (1969).  
[30] C. A. Heusch *et al.*, Phys. Rev. Lett. **25**, 1381 (1970).  
[31] M. Hongoh *et al.*, Lett. Nuovo Cim. **2S2**, 317 (1971).  
[32] A. Christ *et al.*, Lett. Nuovo Cim. **8S2**, 1039 (1973).  
[33] P. S. L. Booth *et al.*, Nucl. Phys. B **71**, 211 (1974).  
[34] L. O. Abramian *et al.*, Pisma Zh. Eksp. Teor. Fiz. **25**, 597 (1977).  
[35] G. A. Vartapetyan and S. E. Piliposian, Sov. J. Nucl. Phys. **32**, 804 (1980).  
[36] S. Homma *et al.*, J. Physical Society Japan **57**, 828 (1988).  
[37] A. Bock *et al.*, Phys. Rev. Lett. **81**, 534 (1998).  
[38] J. Ajaka *et al.*, Phys. Rev. Lett. **81**, 1797 (1998).  
[39] V. Kouznetsov *et al.*, Phys. Rev. Lett. **81**, 1797 (1998).  
[40] J. Ahrens *et al.*, Eur. Phys. J. A **17**, 241 (2003).  
[41] D. Elsner *et al.*, Eur. Phys. J. A **33**, 147 (2007).  
[42] M. Sumihama *et al.*, Phys. Rev. C **80**, 52201 (2009).  
[43] M. Williams *et al.*, Phys. Rev. C **80**, 45213 (2009).  
[44] M. Sikora, Ph.D. dissertation, The University of Edinburgh (2011).  
[45] C. S. Akondi *et al.*, Phys. Rev. Lett. **113**, 102001 (2014).  
[46] I. Senderovich *et al.*, Phys. Lett. B **755**, 64 (2016).  
[47] V. L. Kashevarov *et al.*, Phys. Rev. Lett. **118**, 212001 (2017).

## Appendix A: Final Fits to Experimental Data

Figures 10 - 25 show fits to  $\gamma p \rightarrow \eta p$  and  $\gamma n \rightarrow \eta n$  data for the observables  $d\sigma/d\Omega$ ,  $\Sigma$ ,  $T$ ,  $F$ , and  $E$ . The partial-wave amplitudes used to generate the curves are available in the form of data files [23]. Also shown are the fits from BnGa 2016 [2] and Jülich 2015b [3].

Data sources shown in the plots are: HEUSCH 1966 [24], PREPOST 1967 [25], BACCI 1968 [26], BLOOM 1968 [27], ERBE 1968 [9], DELCOURT 1969 [28], HOLT 1969 [29], HEUSCH 1970 [30], HONGOH 1971 [31], CHRIST 1973 [32], BOOTH 1974 [33], ABRAMIAN 1977 [34], VARTAPETYAN 1980 [35], HOMMA 1988 [36], KRUSHE 1995 [11], PRICE 1995 [12], BOCK 1998 [37], AJAKA 1998 [38], KOUZNETSOV 1998 [39], DUGGER 2002 [13], AHRENS 2003 [40], CREDE 2005 [14], NAKABAYASHI 2006 [15], BARTALINI 2007 [16], ELSNER 2007 [41], SUMIHAMA 2009 [42], WILLIAMS 2009 [43], CREDE 2009 [17], MCNICOLL 2010 [18], SIKORA 2010 [44], AKONDI 2014 [45], SENDEROVICH 2014 [46], WITTHAUER 2017 [7], and KASHEVAROV 2016 [47].

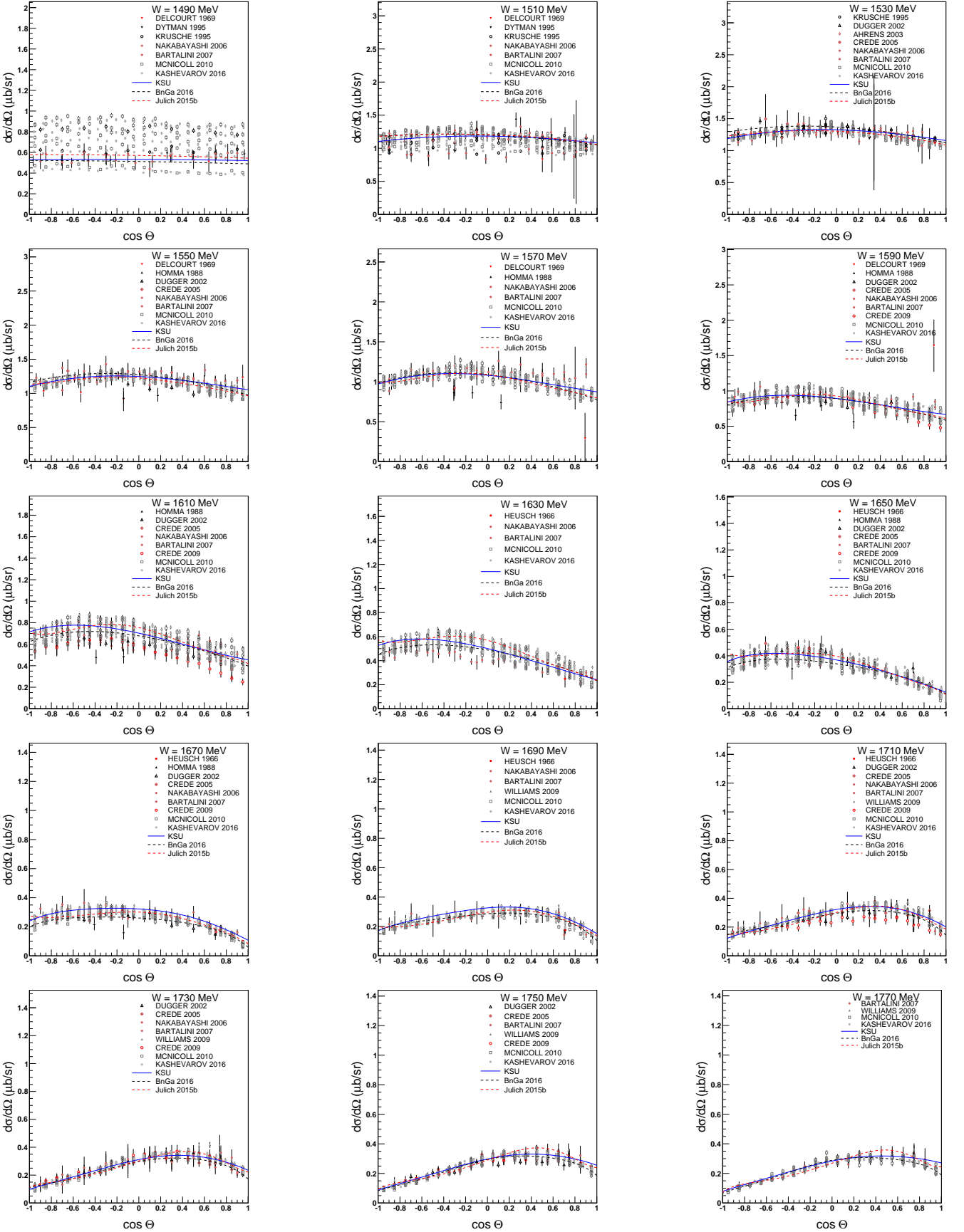


FIG. 10. Fits to  $d\sigma/d\Omega$  data for  $\gamma p \rightarrow \eta p$  at  $W = 1490$  to 1770 MeV. See text for references.

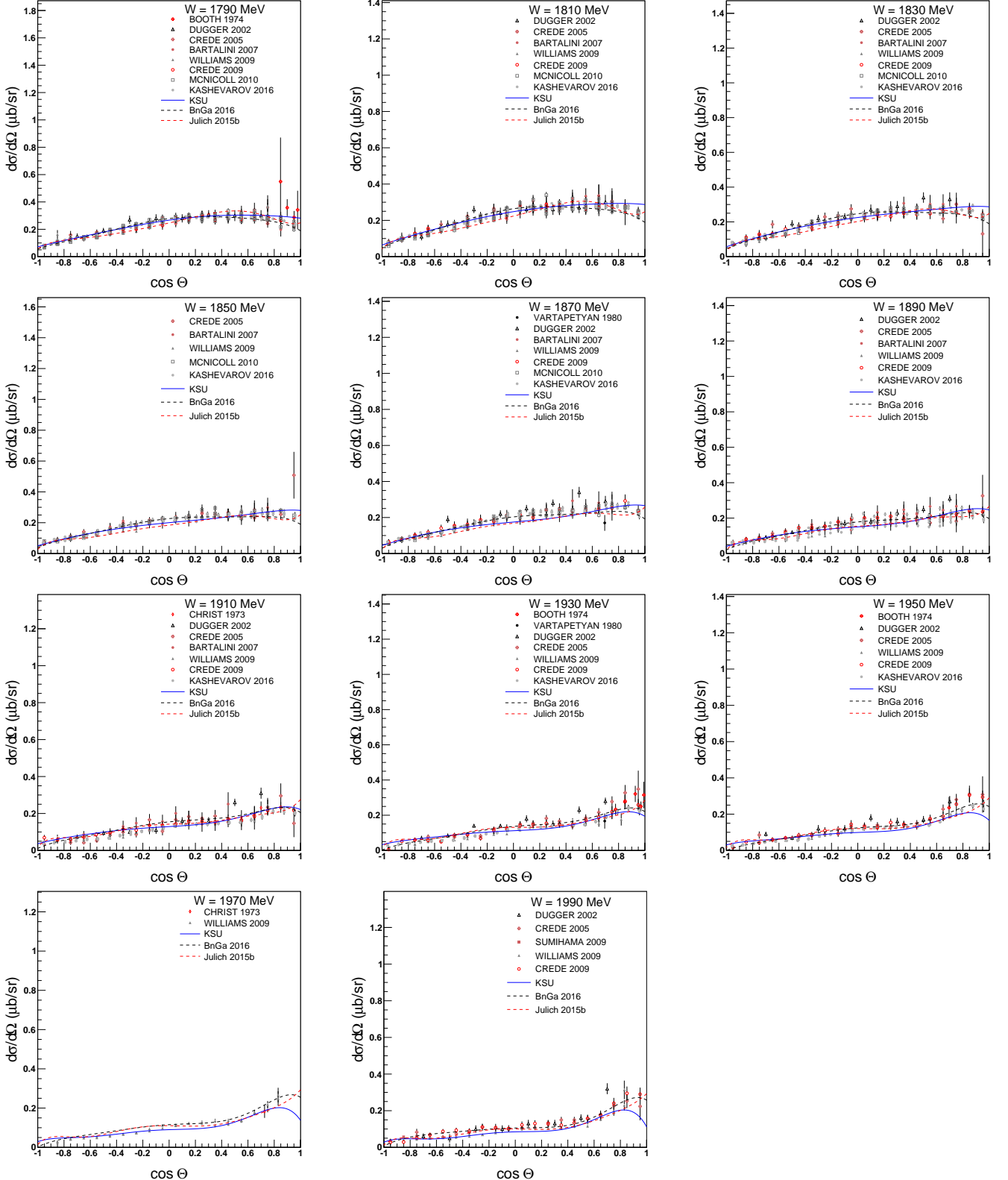


FIG. 11. Fits to  $d\sigma/d\Omega$  data for  $\gamma p \rightarrow \eta p$  at  $W = 1790$  to  $1990$  MeV. See text for references.

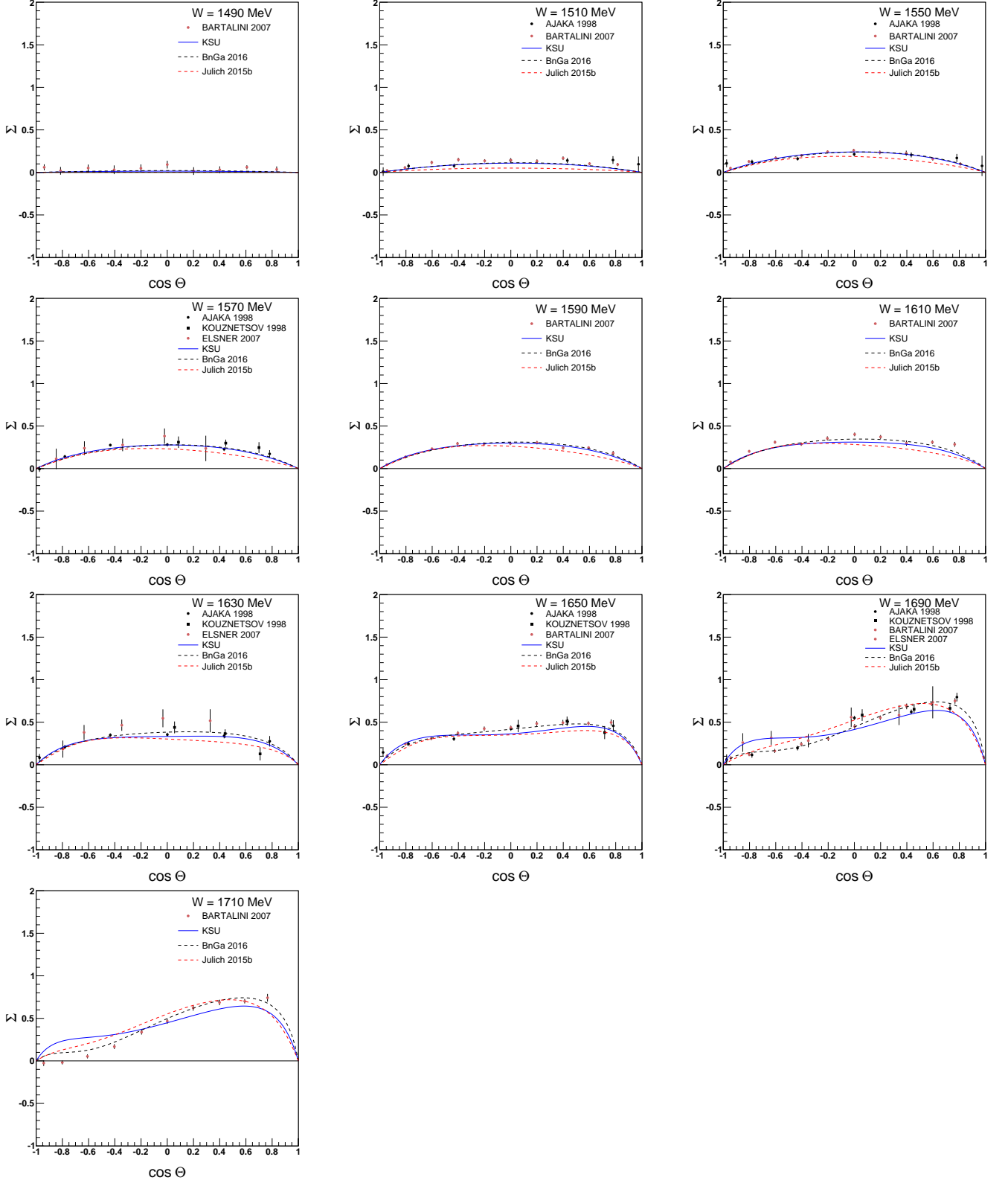


FIG. 12. Fits to  $\Sigma$  data for  $\gamma p \rightarrow \eta p$  at  $W = 1490$  to 1710 MeV. See text for references.

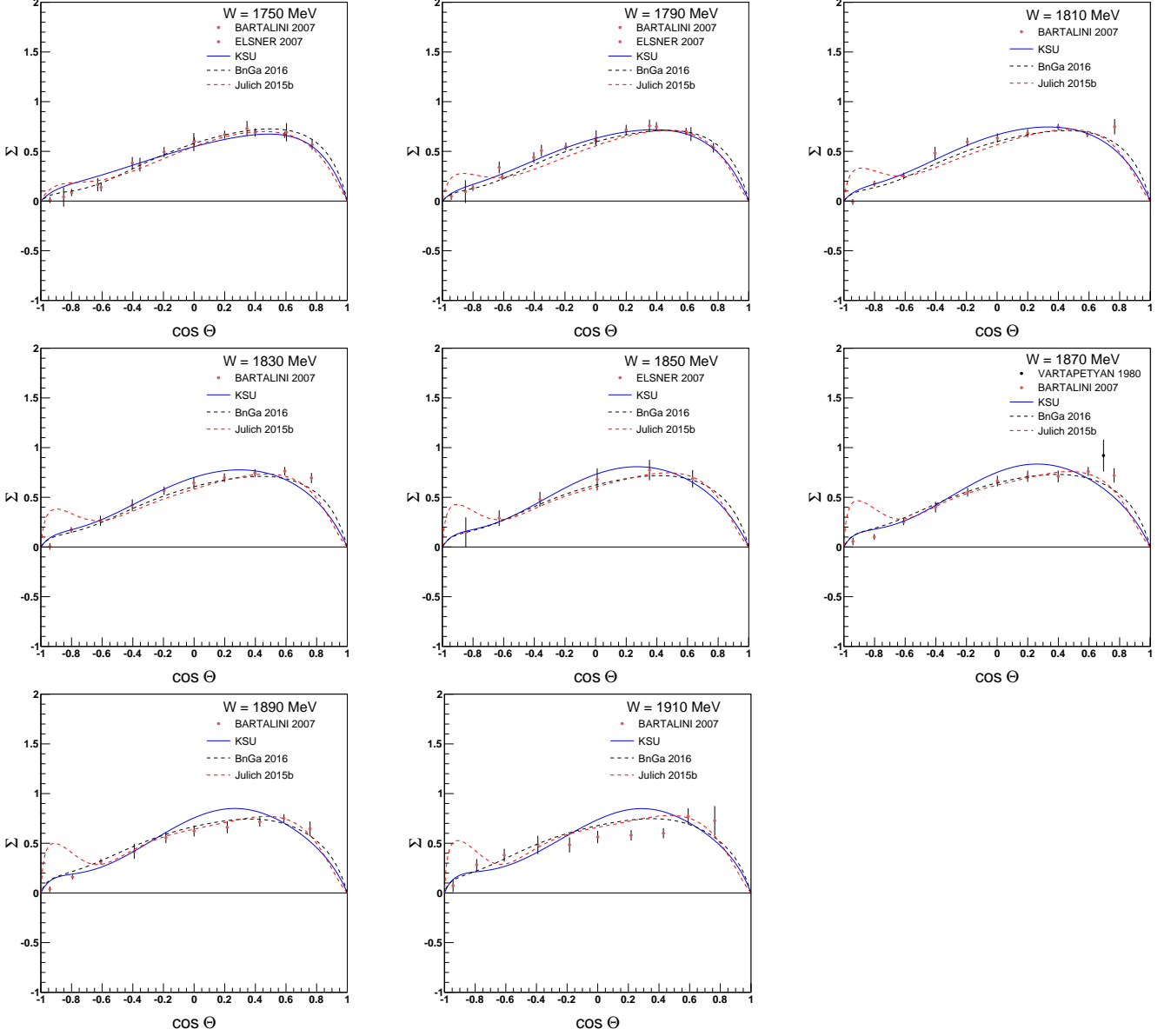


FIG. 13. Fits to  $\Sigma$  data for  $\gamma p \rightarrow \eta p$  at  $W = 1750$  to 1910 MeV. See text for references.

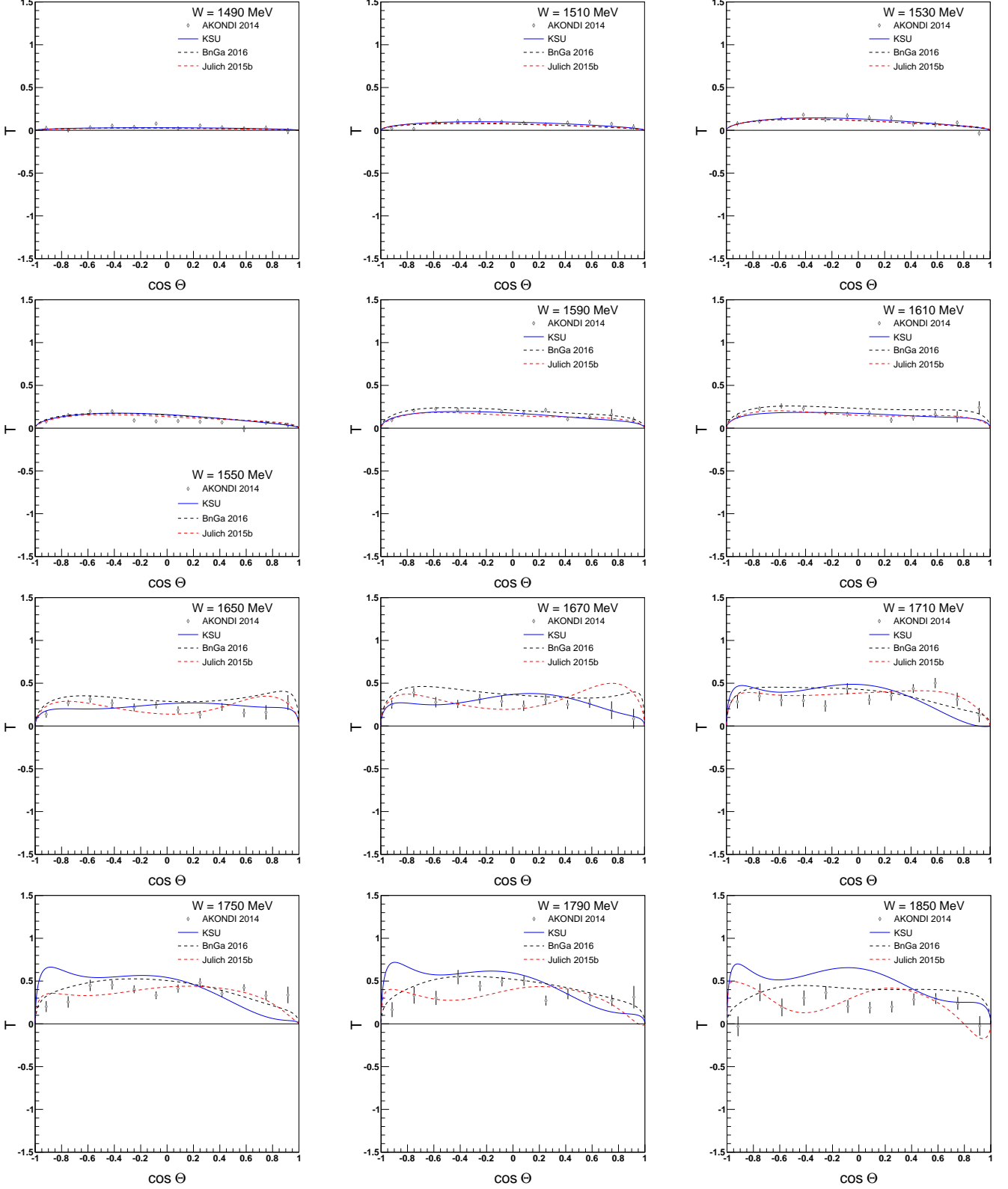


FIG. 14. Fits to  $T$  data for  $\gamma p \rightarrow \eta p$  at  $W = 1490$  to  $1850$  MeV. See text for references.

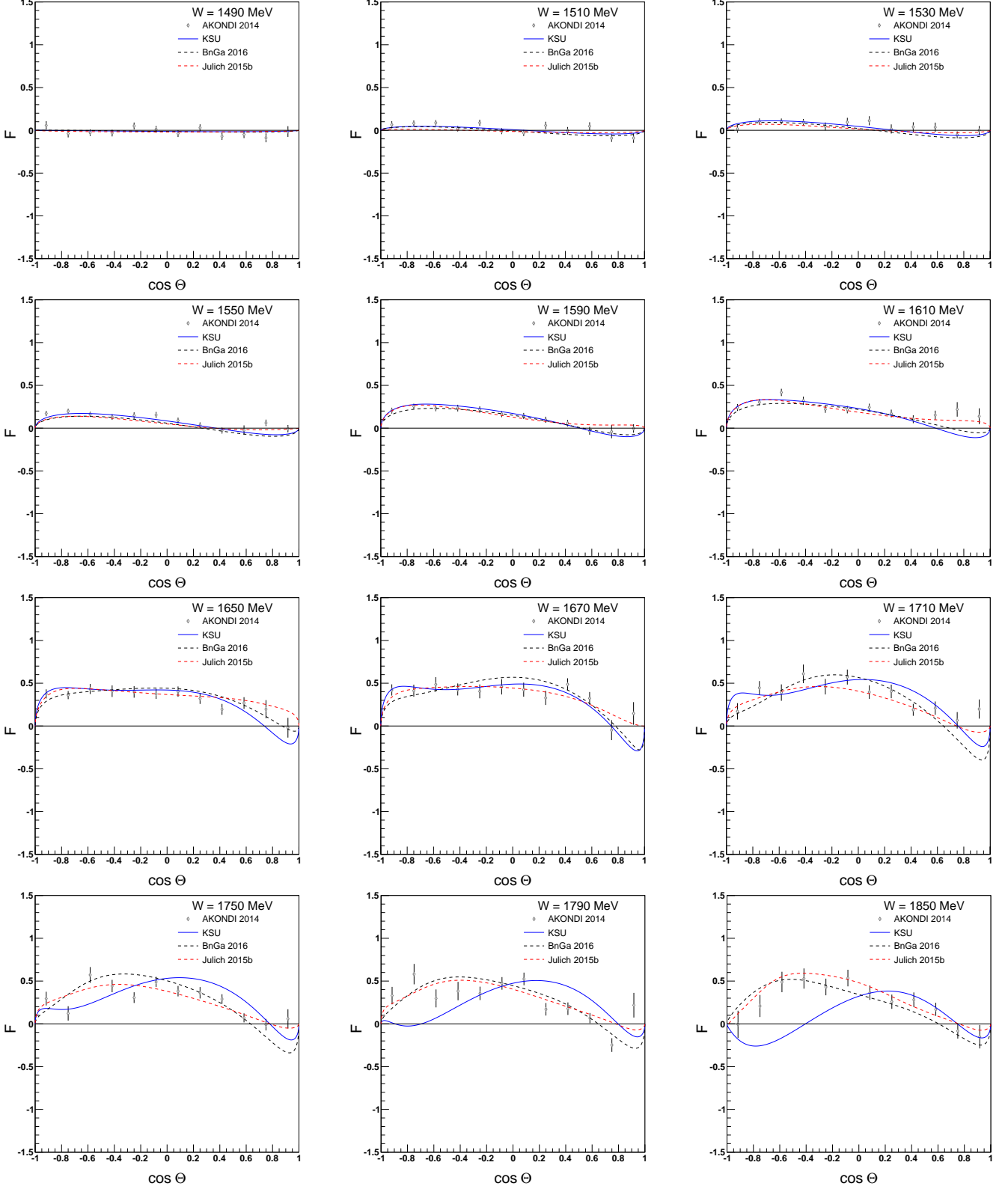


FIG. 15. Fits to  $F$  data for  $\gamma p \rightarrow \eta p$  at  $W = 1490$  to 1850 MeV. See text for references.

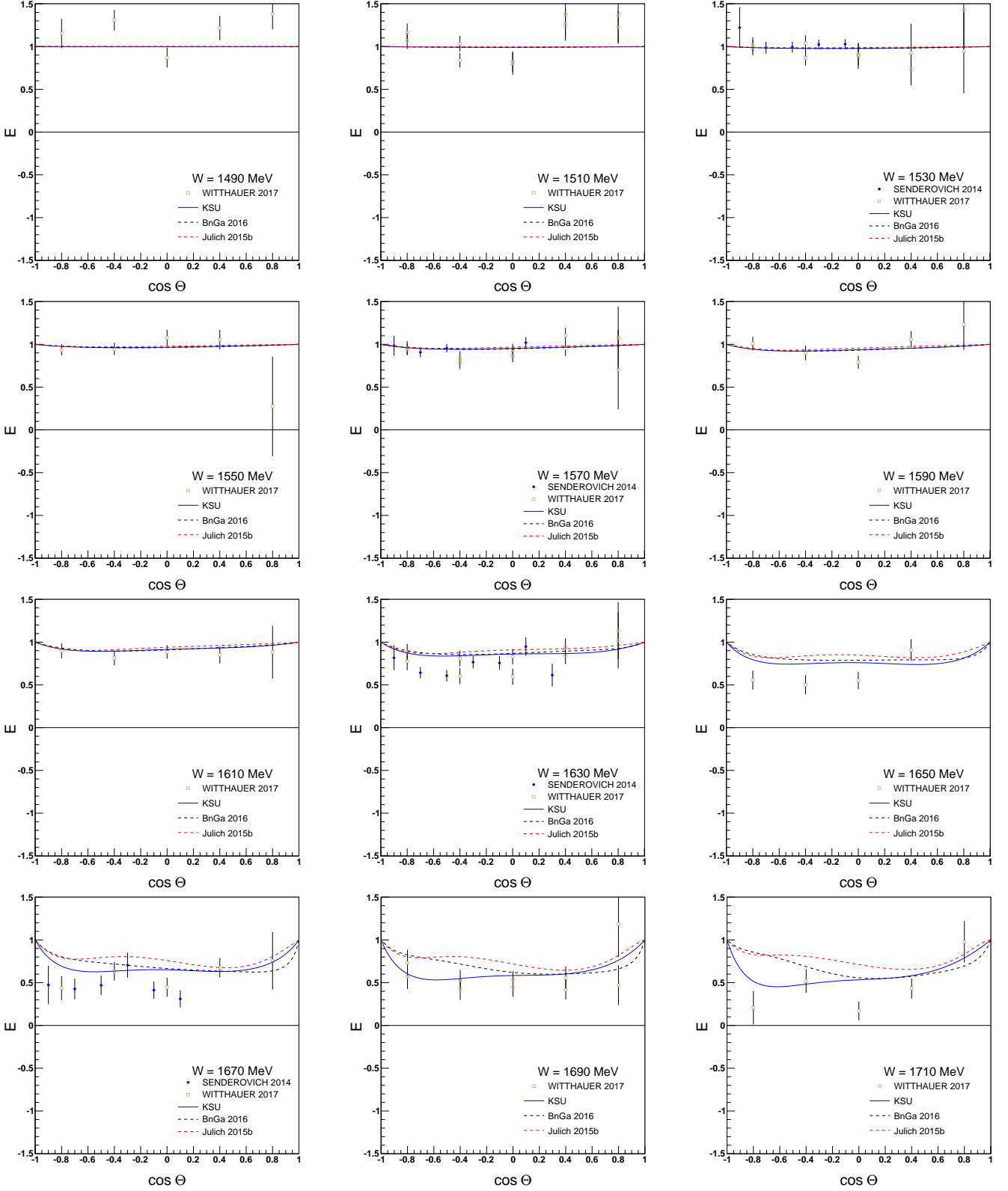


FIG. 16. Fits to  $E$  data for  $\gamma p \rightarrow \eta p$  at  $W = 1490$  to 1710 MeV. See text for references.

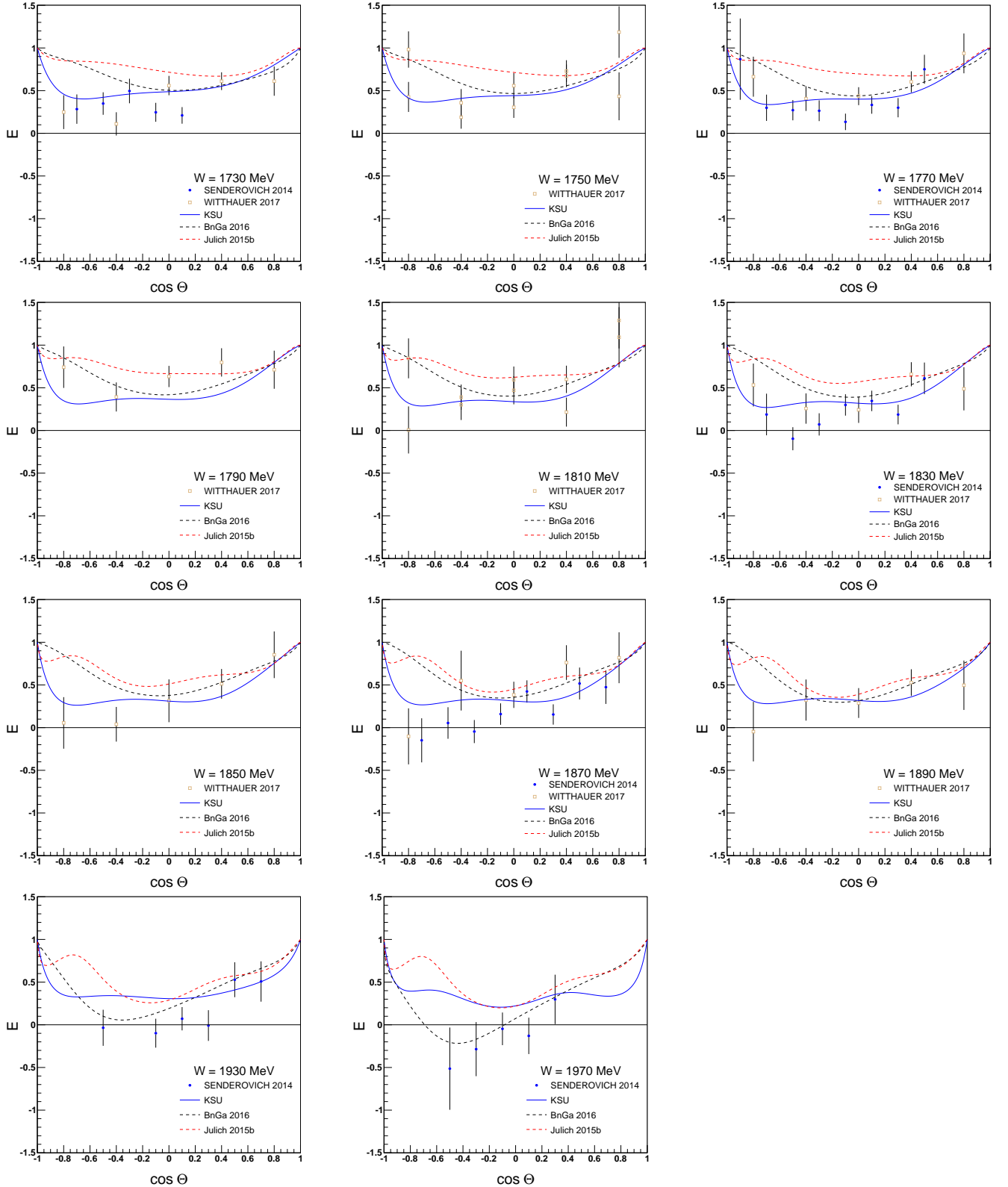


FIG. 17. Fits to  $E$  data for  $\gamma p \rightarrow \eta p$  at  $W = 1730$  to 1970 MeV. See text for references.

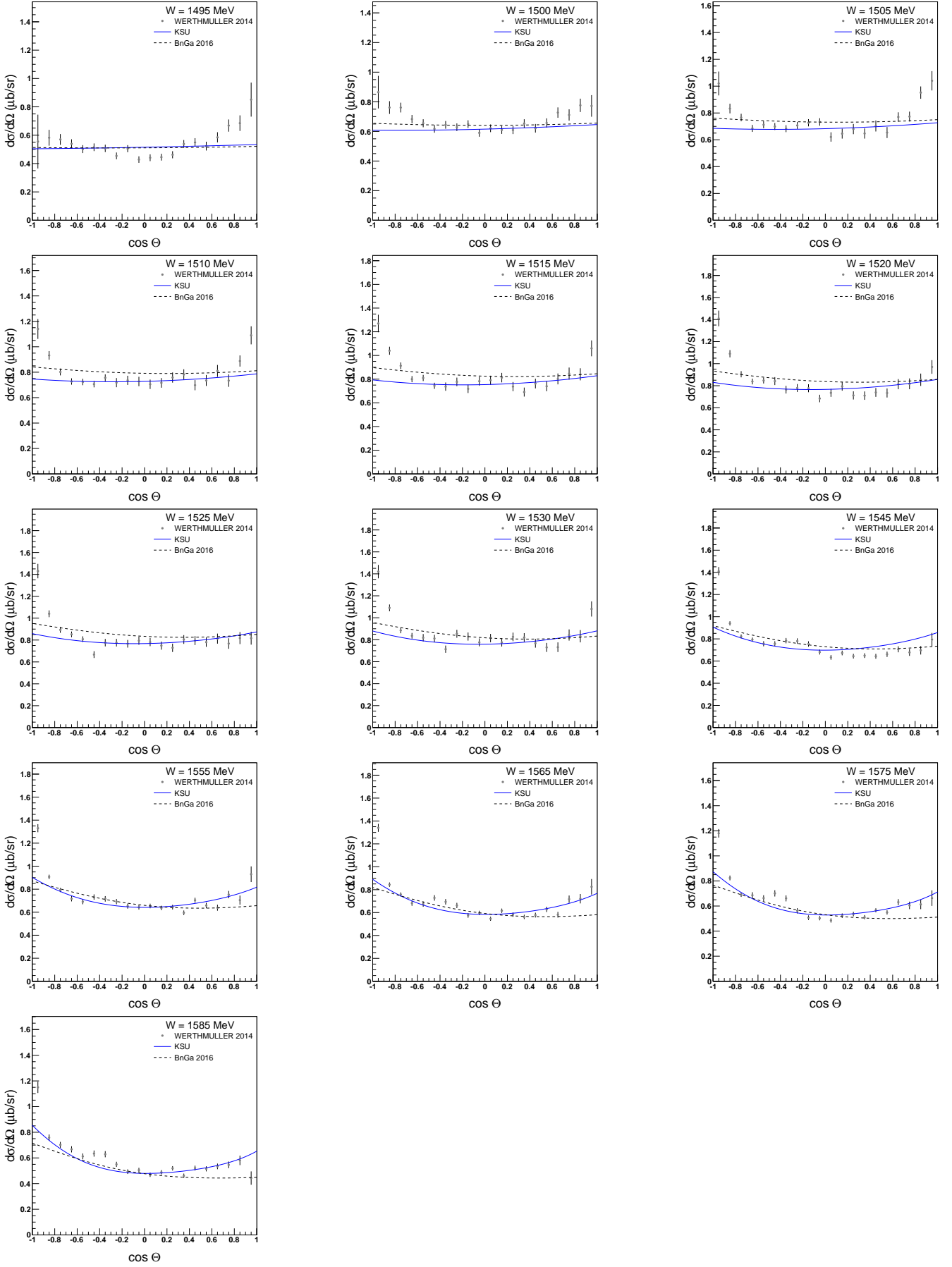


FIG. 18. Fits to  $d\sigma/d\Omega$  data for  $\gamma n \rightarrow \eta n$  at  $W = 1495$  to 1585 MeV. See text for references.

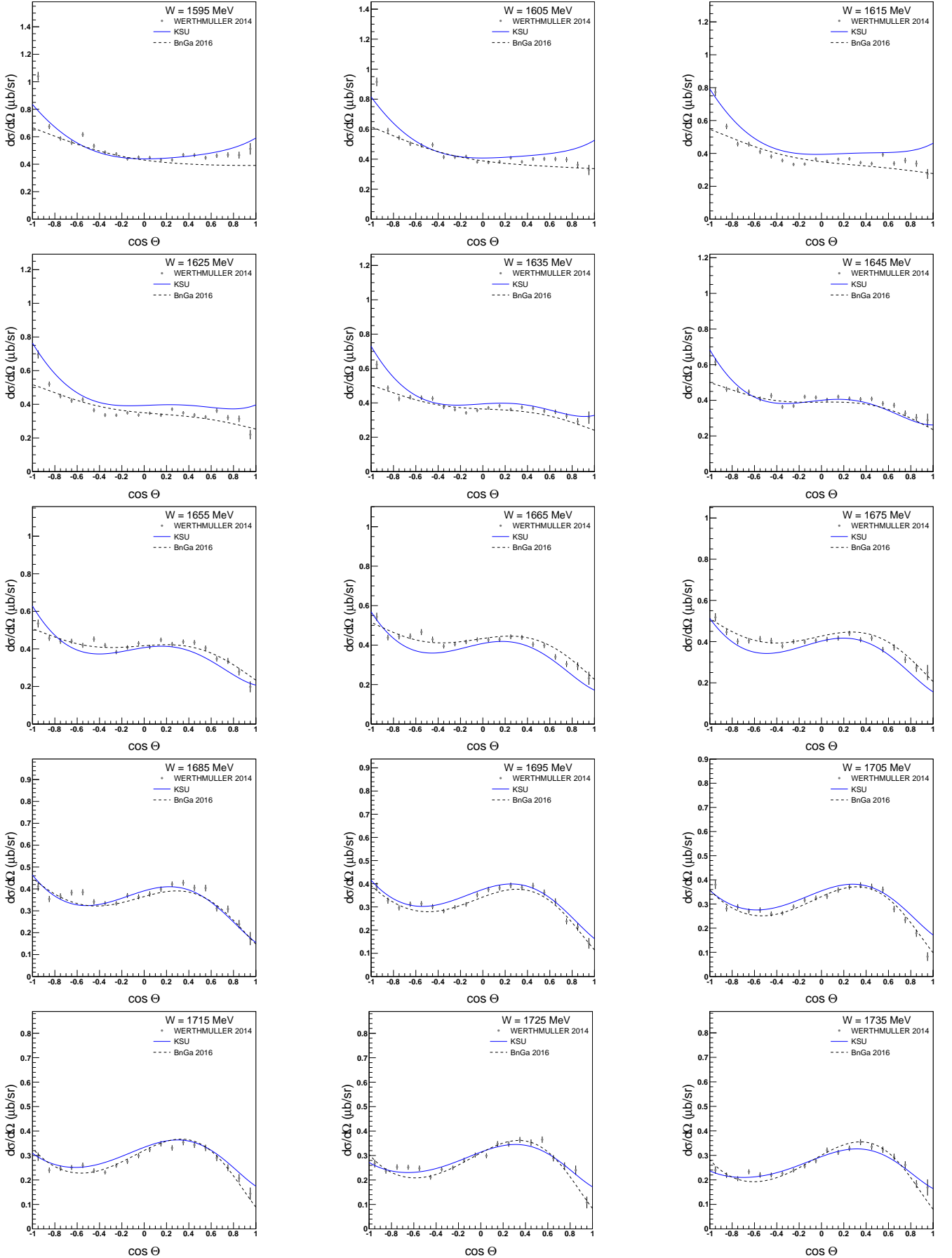


FIG. 19. Fits to  $d\sigma/d\Omega$  data for  $\gamma n \rightarrow \eta n$  at  $W = 1595$  to 1735 MeV. See text for references.

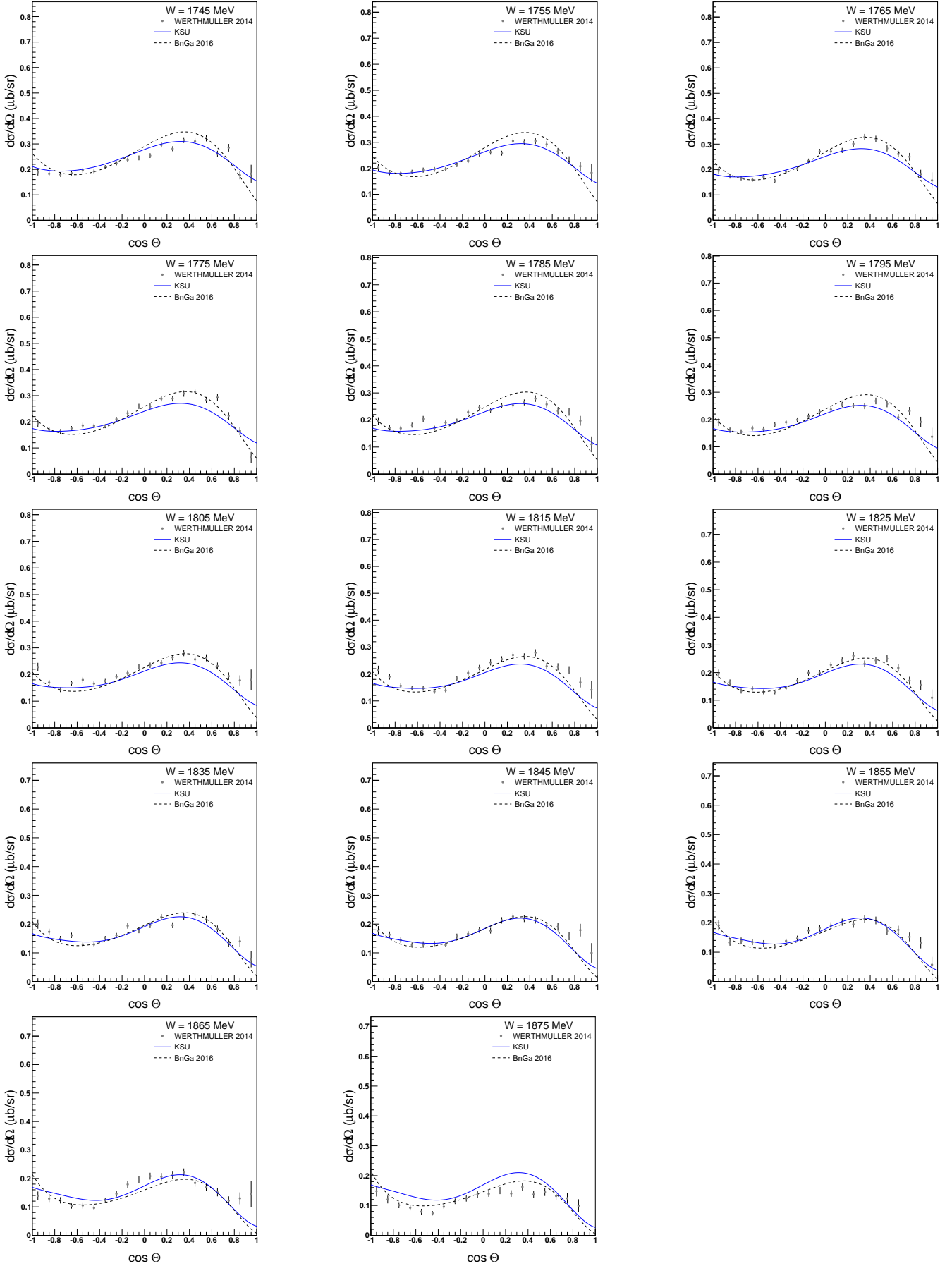


FIG. 20. Fits to  $d\sigma/d\Omega$  data for  $\gamma n \rightarrow \eta n$  at  $W = 1745$  to 1875 MeV. See text for references.

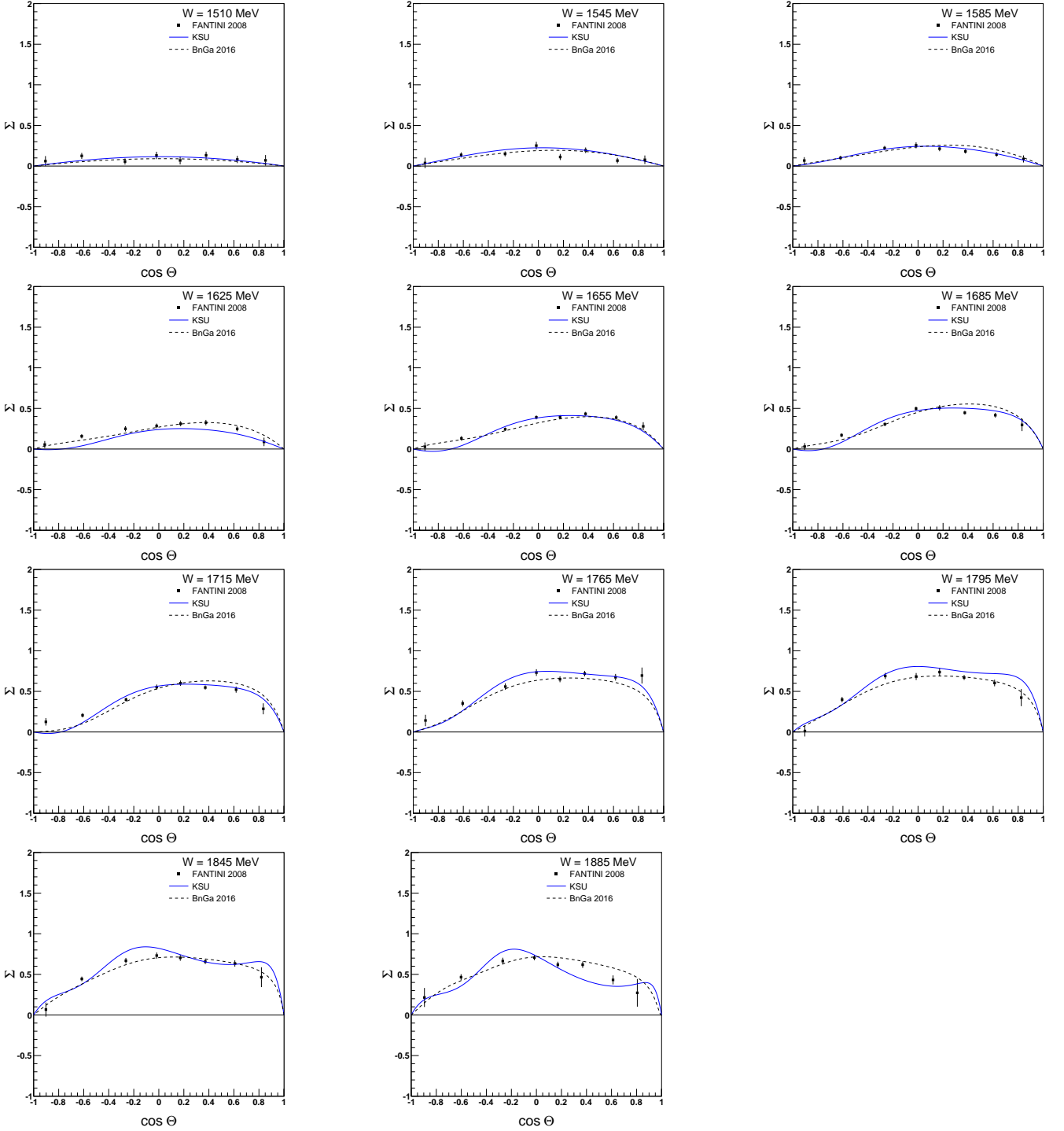


FIG. 21. Fits to  $\Sigma$  data for  $\gamma n \rightarrow \eta n$  at  $W = 1510$  to 1885 MeV. See text for references.

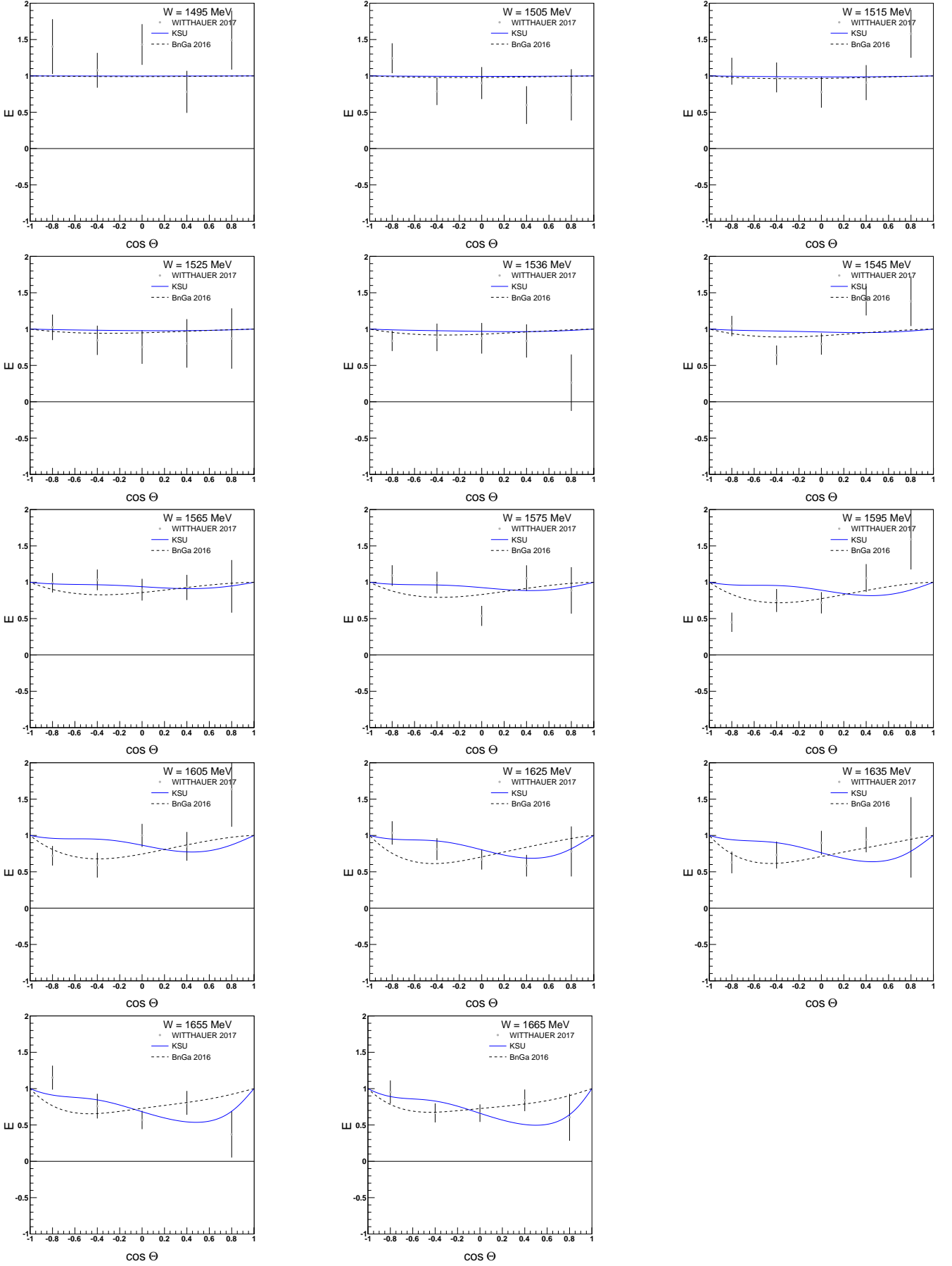


FIG. 22. Fits to  $E$  data for  $\gamma n \rightarrow \eta n$  at  $W = 1495$  to 1665 MeV. See text for references.

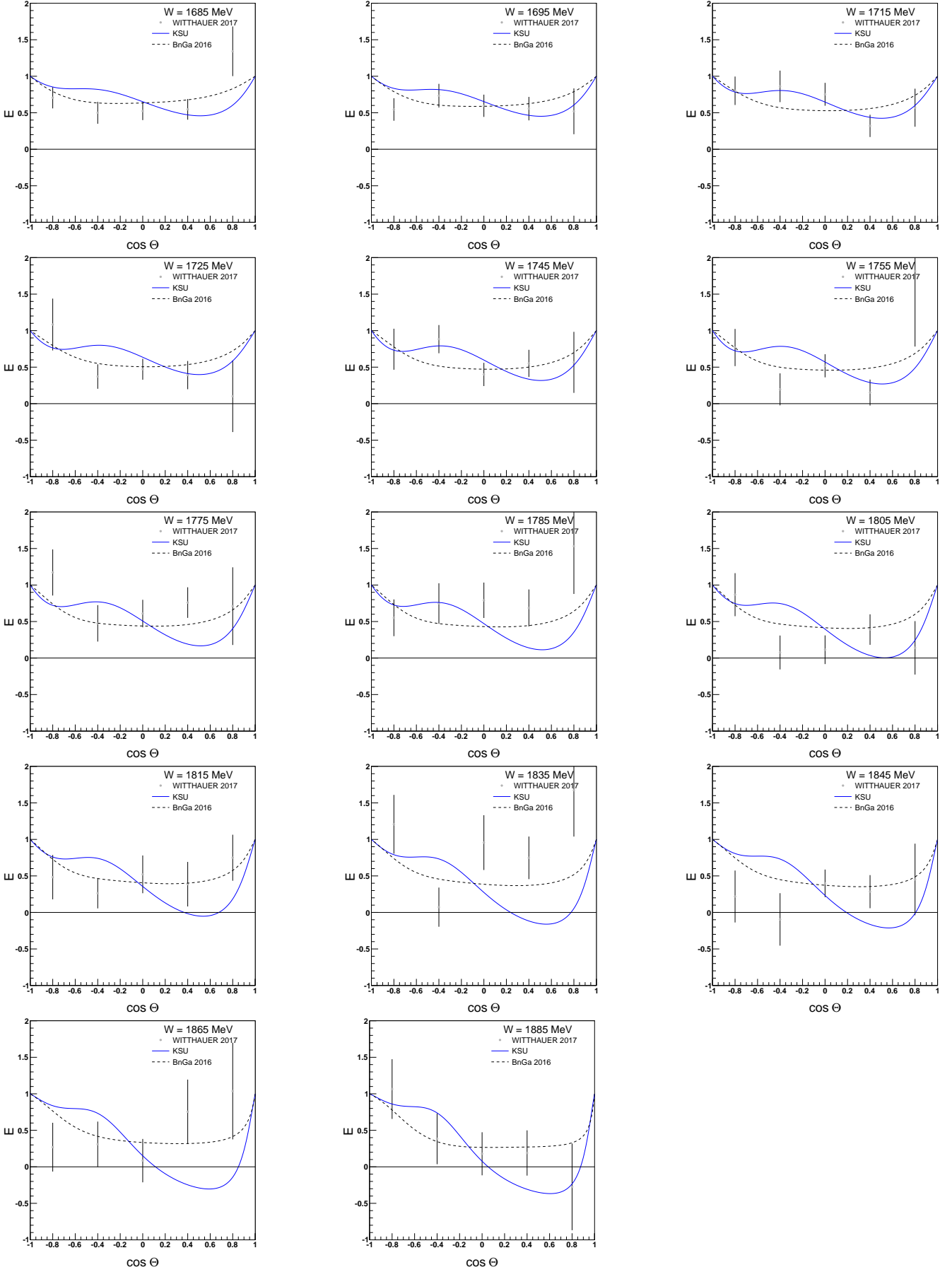


FIG. 23. Fits to  $E$  data for  $\gamma n \rightarrow \eta n$  at  $W = 1685$  to  $1885$  MeV. See text for references.

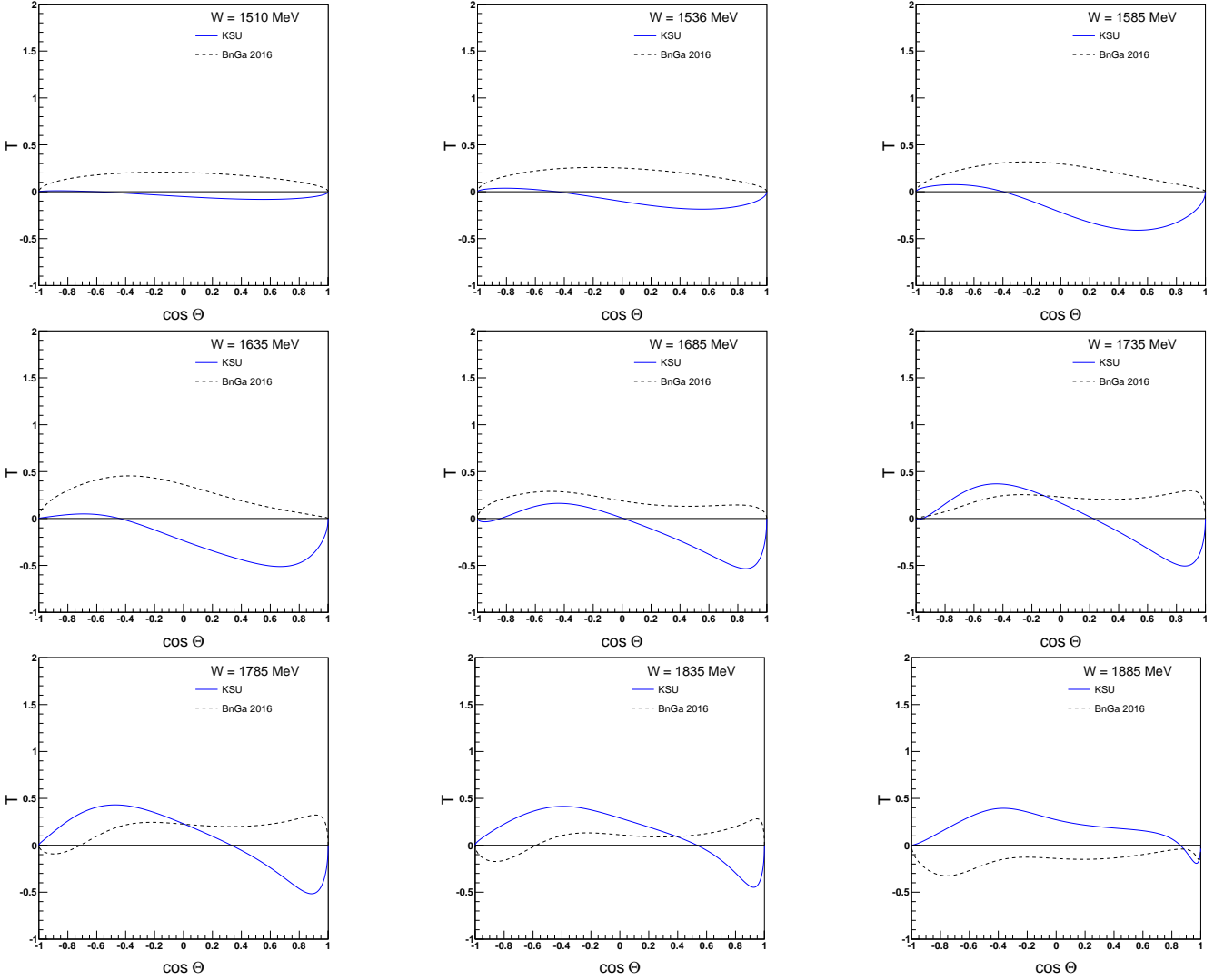


FIG. 24. Fits to  $T$  data for  $\gamma n \rightarrow \eta n$  at  $W = 1510$  to  $1885$  MeV. See text for references.

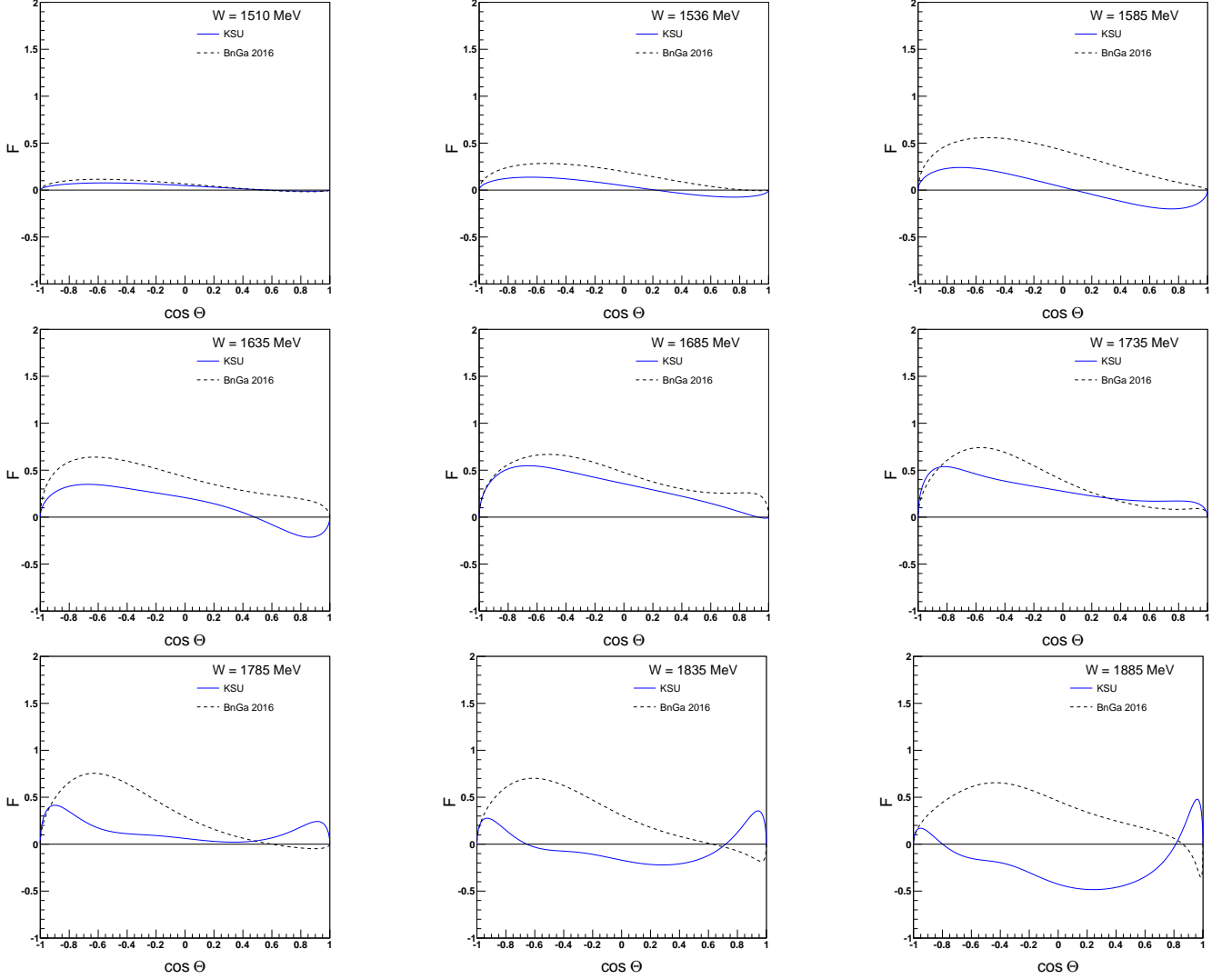


FIG. 25. Fits to  $F$  data for  $\gamma n \rightarrow \eta n$  at  $W = 1510$  to  $1885$  MeV. See text for references.